Deltares

Enabling Delta Life

WTI 2017: Toetsregel piping

Validation piping module DgFlow
(report including primary erosion)

Deltares

WTI 2017: Toetsregel piping

Validation piping module DgFlow
(report including primary erosion)

dr.ir. J.M. van Esch

1220084-004

Deltares

Title
WTI 2017: Toetsregel piping

Client	Project	Reference	Pages
Rijkswaterstaat	1220084-004	1220084-004-GEO-0002-ydh	46

Keywords
Finite element method, Groundwater flow, Piping Dikes Dams

Summary
Dikes and dams are water mitigating structures that protect the land from floods and high tides. In the Netherlands these structures are often constructed of impervious clays and are built on a sandy aquifer as subsoil. Foundations of such geotechnical structures are vulnerable to an erosion effect called piping that refers to the development of small flow channels that begin at the downstream side of the structure where the seepage pressure is high. The internal erosion process works its way to the upstream side, and if the erosion process continues the structure may collapse.
Failure due to piping is a risk for many river levee systems. In the Netherlands, piping is the dominant failure mechanism. The prediction of this phenomenon has therefore received much attention in the past and is still being investigated. Starting with simple empirical rules in the beginning of previous century, with ongoing research the prediction models have become more physics based, and are often founded or calibrated using experimental data. At present the most advanced design rule for piping is the rule proposed by Sellmeijer (1988).However, Sellmeijer's model does not describe the hole piping process sufficiently. The deficiencies gave reason to develop the finite element groundwater flow model DgFlow. This enables modeling of all erosion processes concerning piping in one tool, taking into account effects like time-dependent loads and heterogeneity of the subsoil.
This report presents the verification and validation of DgFlow. Verification tests show the resemblance of the results of numerical computations and the outcome of Sellmeijer's rule. Validation tests compare the outcome of the numerical computations with laboratory observations. The DgFlow computations provide a critical value that is about 1.5 times smaller than the observed value in the laboratory. Increasing the grain size by a factor 1.5, or increasing the pipe width by a factor $(1.5)^3$ or decreasing the permeability of the medium by a factor $(1.5)^3$ increases the computed critical head by a factor 1.5 and provides critical heads that compare reasonably well with experimental results. However, the observed parameters (grain diameter, pipe width and permeability) are not within this range of variation and a correction could not be justified. For this reason the current report focusses on the primary erosion process, which also increases the critical head.
This report presents an approach to model primary erosion in the prediction model. Furthermore an improvement was made to the secondary erosion criterion by setting the width of the channel as a function of the channel height.

Version	Date	Author	Initials	Review	Initials	Approval	Initials
1	Sept. 2015	dr.ir. J.M. van Esch		ir. V.M. van Beek		ir. L Voogt	

State final

Contents

1 Introduction

In delta regions dikes protect the land from floods and high tides. In the Netherlands dikes are generally constructed of impervious clays and are built on a sandy aquifer as subsoil. The foundations of these geotechnical structures are vulnerable to an erosion process called piping. Piping is a form of seepage erosion where groundwater flow affects the soil stability. In literature, the piping mechanism is also referred to as backward erosion or underseepage erosion (Lane (1935); Wolfs (2002)). Figure 1.1 illustrates the piping process for a cross section of a dike on a low permeability holocene layer, which covers a pleistocene high permeability aquifer.

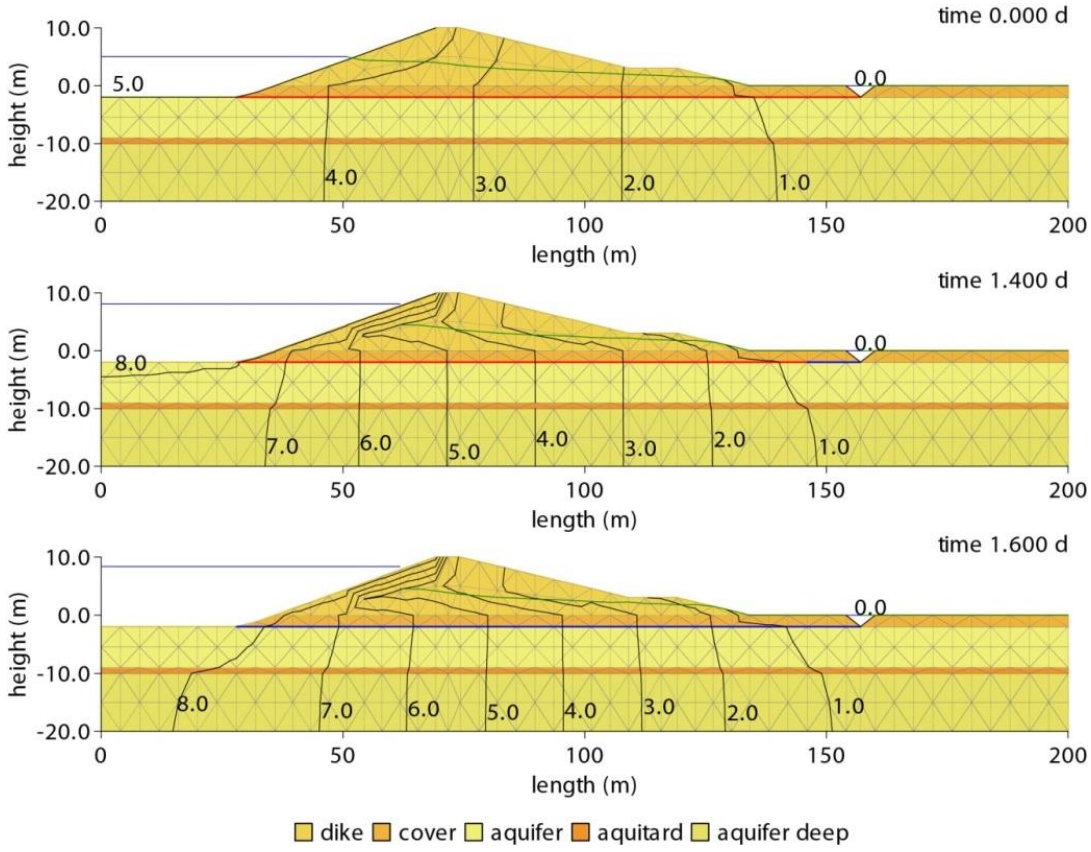

Figure 1.1 Piping under a dike, indicated by the blue line at the base of the embankment.

The blue line displays the free water level at the river side, and the green line presents the phreatic surface in the dike. In this configuration seepage occurs at the lower end of the berm, where the green line intersects the dike surface. The black lines present the decline of the hydraulic head in the aquifer from the river side to the polder. The top picture shows the initial situation where, given the head difference over the structure, there is no piping channel

under the dike. This is indicated by the red line at the base of the structure. The middle picture shows a stable active piping channel of 12 meters due to the increased head difference over the structure. The active piping channel is indicated by the blue part of the base line. The bottom picture finally shows a piping channel that extends to the upstream side. This situation was obtained for a head difference that exceeds the critical head difference related to the piping mechanism.

For the piping mechanism four phases can be distinguished; the initiation phase, the equilibrium phase, the progressive phase, and the widening phase. The initiation phase starts the process. If the water pressure underneath the cover layer exceeds the weight of the cover layer then uplift conditions apply, the cover layer might crack and preferential flow lines will develop through the subsoil. This will start a concentrated groundwater flux and small sand boils at the downstream exit point will develop. This initial phase is also known as the boiling phase where sand boils without the deposition of sand. Further increase of head leads to pipe formation causing the sand boils to transport and deposit sand. In the equilibrium phase small channels that begin at the sand boils, where the seepage pressure is high, develop towards the upstream side and the sand boils grow as more material is transported out of the subsurface. In this phase of the process the erosion channel has a finite length smaller than the construction length and grains in the channels are in equilibrium. If the head difference over the structure increases then the propagation of erosion channels continues and the small channels grow in size. In the progression phase the pipe develops towards the upstream side. At the moment the piping channel reaches the upstream side the material transport strongly increases. This is known as the widening phase. Finally the structure may collapse and then water overflows the dike.

Failure due to piping is a risk for many river levee systems. The prediction of this phenomenon has therefore received much attention in the past and is still being investigated. Starting with simple empirical rules in the beginning of previous century, with ongoing research the prediction models have become more physics based, and are often founded or calibrated using experimental data. In the Netherlands these prediction models are used to perform a 12-yearly safety assessment of primary water-retaining structures. To perform the safety assessment, an assessment protocol (WTI) is determined by the secretary of Infrastructure and the environment, consisting of the Voorschrift Toetsen op Veiligheid (VTV) and Hydraulische Randvoorwaarden (HR). To improve prediction models for increased safety and optimal reinforcement of levees, the research program SBW (Strength and loads on Flood defense structures) has been initiated.

At present the most advanced design rule for piping is the rule proposed by Sellmeijer (1988). However Sellmeijer's model does not describe the hole piping process sufficiently. These deficiencies gave reason to develop the finite element groundwater flow model DgFlow. This enables modeling of all erosion processes concerning piping in one tool, taking into account effects like time-dependent loads and heterogeneity of the subsoil.

This report extends the piping module of the groundwater flow simulator DgFlow to 3D and validates the module. DgFlow was developed as part of the safety assessment program (WTI2017), which is funded by the Rijkswaterstaat. Rijkswaterstaat is part of the Dutch Ministry of Infrastructure and the Environment and responsible for the design, construction, management and maintenance of the main infrastructure facilities in the Netherlands. Chapter 2 presents the groundwater flow model by presenting its mathematical formulation and numerical solution. Chapter 3 discusses the sand box experiments conducted by Van Beek ea. (2014a) that will be used for verification and validation of the model. A verification study compares the outcome of the 2D Sellmeijer's rule with DgFlow computational results for a two-dimensional flow problem that was set up in a 3D domain. Validation of the DgFlow model is based on the set of 3D laboratory experiments. This report is an extension of the report presented by Van Esch (2014); a criterion for primary erosion is suggested and implemented in DgFlow and in addition the modeling of secondary erosion is improved by applying a constant width to depth ratio. Chapter 4 presents the conclusions.

2 Groundwater flow simulator

The finite element code DgFlow simulates the interaction of groundwater flow and the development of piping channels underneath a dike. The formulation of the piping mechanism is based on Poiseuille flow through a rectangular piping duct and White's limit equilibrium for particle movement. A prediction of transient groundwater flow and the associated groundwater pressure field follows from the solution of the Richard's equation. This chapter presents the mathematical formulation and the numerical solution of the piping mechanism and groundwater flow that forms the basis of DgFlow.

2.1 Mathematical model

Sellmeijer's model applies a single particle approach for which the transport equations consider equilibrium of forces. The forces that are taken into account are the gravitational force and the drag force. The force due to the vertical hydraulic gradient and the force due to the horizontal gradient are neglected. The model assumes that the grain is at rest if the drag force does not exceed the counteracting gravitational force. This is the case if the shear stress exerted by the water is less than the critical shear stress $\tau_c \ (\mathrm{N/m^2})$, which reads

$$\tau_c = \frac{\pi}{6}\left(\rho^s - \rho^l\right) g \eta d_c \tan\vartheta \tag{2.1}$$

Here $\rho^s \ (\mathrm{kg/m^3})$ corresponds to the density of the soil particles, $\rho^l \ (\mathrm{kg/m^3})$ denotes the density of the water phase, η (-) expresses White's constant, ϑ (deg) is the bedding angle, and d_c (m) denotes a characteristic grain diameter.

White's parameter η was set to 0.25 and accounts for the uptake of shear stress of a single particle in a sand bed. For larger values of the shear force, its component parallel to the grain interface will be larger than the gravitational force in that direction and the particle will move.

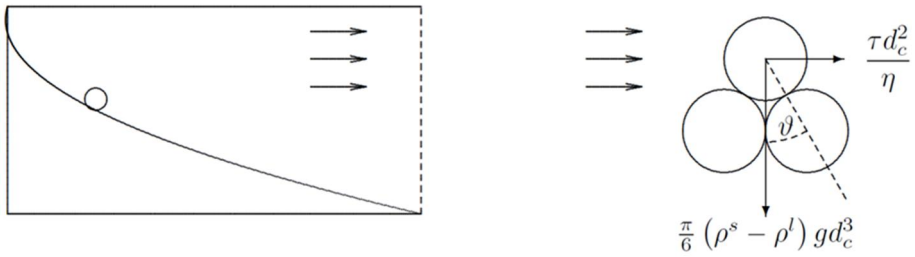

Figure 2.1 Grain equilibrium according to Sellmeijer

Figure 1.2 shows both forces acting on a single grain. Here the bedding angle ϑ approximately represents the maximum slope of a pile of grains under water.

The actual shear stress exerted by the water depends on the height of the channel a (m) and the pressure gradient along the pipe. This shear stress can be expressed as

$$\tau = \frac{a}{2}\frac{dp}{dx} \tag{2.2}$$

A combination of Equations (2.1) and (2.2) specifies the limit state equilibrium according to

$$a\frac{dp}{dx} = \frac{\pi}{3}\left(\rho^s - \rho^l\right)\eta g d_c \tan\vartheta \tag{2.3}$$

Subsurface flow equation

Flow through a partly saturated porous medium can be modeled considering conservation of mass and a generalization of Darcy's law, which can be written as

$$\left(\alpha + n\beta\right)S\frac{\partial p}{\partial t} + n\frac{dS}{dp}\frac{\partial p}{\partial t} + \frac{\partial q_i}{\partial x_i} = 0\,, \quad q_i = -\frac{k_r \kappa_{ij}}{\mu^l}\left(\frac{\partial p}{\partial x_j} - \rho^l g_j\right) \quad \text{on} \quad \Omega^p\,, \tag{2.4}$$

where α $(\mathrm{m}^2/\mathrm{N})$ is the compressibility of the soil skeleton, β $(\mathrm{m}^2/\mathrm{N})$ represents the compressibility of the pore water, n (-) denotes porosity and S (-) expresses the degree of saturation of the liquid phase in the void space. The compressibility in the case of elastic behavior of the soil skeleton can be written as $\alpha = 1/(\lambda + 2\nu)$, where λ $(\mathrm{N/m}^2)$ and ν $(\mathrm{N/m}^2)$ denote Lamè's constants. Specific discharge q_i $(\mathrm{m/s})$ relates to relative

permeability k_r (-), intrinsic permeability κ_{ij} (m^2), dynamic viscosity of the liquid phase μ^l $(\mathrm{kg/ms})$ and its density ρ^l $(\mathrm{kg/m}^3)$. For a y-coordinate pointing in the opposite direction than the gravitational vector g_y is -9.81 $\mathrm{m/s}^2$. Equation (2.4) is known as the storage equation.

Constitutive equations for the degree of saturation of a fluid in a porous medium are based on the capillary pressure. The capillary pressure p_c $(\mathrm{N/m}^2)$ denotes the difference of the non-wetting and the wetting phase pressure as $p_c = p^g - p^l$. For liquid-gas flow systems the liquid phase is the wetting phase and the gas phase represents the non-wetting phase. If the gas phase is stagnant, the pressure in the gas phase is constant and equals the atmospheric pressure if the phase is continuous. Then, $p_c = -p^l$ holds for unsaturated conditions and $p_c = 0$ applies for saturated conditions. Van Genuchten and Brooks-Corey (Aziz and Settari, 2002) simplified this by an empirical relation $p_c = p_c(S)$, where S denotes the saturation of the wetting phase, as can be found in Vogel et al. (2001) and Aziz and Settari (2002). Reversely, Van Genuchten-Mualem expresses the saturation as a functional relation of wetting phase pressure according to $S = S(p)$. The Van Genuchten model is written as

$$S = S_r + (S_s - S_r)\left[1 + |g_a \psi|^{g_n}\right]^{-g_m} \quad \text{if} \quad \psi < \psi_a, \qquad S = S_s \quad \text{for} \quad \psi \geq \psi_a, \qquad (2.5)$$

where ψ (m) denotes the pressure head, which reads $\psi = p^l / \rho^l g$, ψ_a (m) is the air-entry pressure head, which is constrained by $\psi_a \leq 0$. S_r (-) is the minimal saturation and S_s (-) denotes the maximum degree of saturation. The minimal saturation deviates from zero due to chemically attached water or entrapped water pockets. The maximum degree of saturation is less than one mainly as a result of entrapped air. The Van Genuchten relation counts two empirical shape factors that have to be measured in the laboratory: g_n (-), and g_a $(1/\mathrm{m})$. For convenience a third shape factor g_m (-) was introduced as $g_m = (g_n - 1)/g_n$. Mualem-Van Genuchten and Brooks-Corey proposed empirical relations for the relative permeability, which also can be found in Vogel et al (2001) and Aziz and Settari (2002). The Van Genuchten relation reads

$$k_r = (S_e)^{g_l}\left[1-\left(1-S_e^{1/g_m}\right)^{g_m}\right]^2, \qquad S_e = \frac{S-S_r}{S_s-S_r}, \tag{2.6}$$

where the empirical shape factor g_l (-) is often set to 0.5. DgFlow adopts the Van Genuchten model because this model is generally used in engineering practice.

Two types of boundary conditions complete the problem definition; Dirichlet conditions prescribe the pressure on parts of the boundary and Von Neumann boundary conditions prescribe the derivative of the pressure or flux on the boundary. These first-type and second-type boundary conditions read

$$p = \bar{p} \quad \text{on} \quad \Gamma_1^p, \quad q_i n_i = -\bar{q} \quad \text{on} \quad \Gamma_2^p, \quad q_i n_i = -s \quad \text{on} \quad \Gamma_3^p, \tag{2.7}$$

where Γ_1^p, Γ_2^p and Γ_3^p are disjoint parts of the boundary where the conditions apply, n_i (-) denotes the outward pointing normal to the boundary, $\bar{p}$ $(\mathrm{N/m^2})$ represents the prescribed pressure, $\bar{q}$ $(\mathrm{m/s})$ denotes the volumetric water flux over the boundary into the flow domain as a source term, and s $(\mathrm{m/s})$ expresses a source term that will be used for coupling the subsurface flow equation to the flow equation for piping. In the current implementation these boundary conditions are generalized to seepage conditions where outflow only occurs under saturated conditions and inflow is prevented. Seepage conditions in turn can be extended to submerging conditions where free water level variations are taken into account, infiltration conditions that simulate precipitation and over-topping conditions, and evaporation conditions.

Pipe flow equation

If flow through a small channel is modeled in one dimension (within a 2D or 3D flow domain) then the flow equation for the pipes follows from the application of conservation of mass and Poiseuille flow as

$$\frac{dq}{dx} + s = 0, \quad q = -\frac{a^2}{12\mu}\frac{dp}{dx} \quad \text{on} \quad \Omega^c, \tag{2.8}$$

In this equation s $(1/\mathrm{s})$ expresses a sink term (Huyakorn and Pinder (1983)) and a (m) denotes the height of the channel. An artificial permeability $\kappa^* = a^2/12$ could be used to transform Poisseuille flow into Darcy flow. The total flow through a rectangular duct then follows from multiplication by the height and the width of the channel as $Q = abq$, where b (m) denotes the width of the channel for three dimensional applications and simply reads $Q = aq$ for a two dimensional cases. In equation (2.8) the extension of the pipe flow domain Ω^c (m) links to the boundary of the subsurface flow domain Γ_3^p (m) in equation (2.7). Dirichlet conditions hold on the inflow and outflow point of the piping domain. Boundary conditions for the piping domain are given by

$$p = \bar{p} \quad \text{on} \quad \Gamma_1^c \,. \tag{2.9}$$

The condition of limit equilibrium for the horizontally oriented erosion channel according to Sellmeijer (1988) reads

$$a\frac{dp}{dx} = \frac{\pi}{3}\left(\rho^s - \rho^l\right) g d_{70} \eta \tan\vartheta \,. \tag{2.10}$$

The height of the erosion channel generally varies between 0 and 3 grains in an experimental setup, 0 to 10 grains in a field test and 0 to 30 grains for an embankment.

The set of equations given by (2.4) and (2.8) is solved numerically (Van Esch ea., 2013a), which could be extended by including soil deformation (Van Esch ea., 2013b). The limit equilibrium condition (2.10) is satisfied sequentially, where the equations are closed by equation (2.7) and (2.9).

2.2 Numerical model

A weak form of equation (2.4) follows from multiplication by weighting functions N_a (-), which are attached to nodes of a finite element mesh, and integration over the flow domain. Application of Green's theorem, Galerkin weighting, substitution of the interpolation functions, incorporation of Neumann boundary conditions and implicit time integration yields

$$\int_{\Omega^p} N_a N_b \left(\alpha + n\beta\right) S^{r+1} \left(p_b^{r+1} - p_b^r\right) d\Omega + \int_{\Omega^p} N_a N_b n \left(\frac{dS}{dp}\right)^{r+1} \left(p_b^{r+1} - p_b^r\right) d\Omega =$$

$$-\Delta t \int_{\Omega^p} \frac{k_r^{r+1} \kappa_{ij}}{\mu} \frac{\partial N_a}{\partial x_i} \frac{\partial N_b}{\partial x_j} p_b^{r+1} d\Omega + \Delta t \int_{\Omega^p} \frac{k_r^{r+1} \kappa_{ij}}{\mu} \frac{\partial N_a}{\partial x_i} \rho^l g_j d\Omega$$

$$+ \Delta t \int_{\Gamma_2^p} N_a N_b \bar{q}_b^{r+1} + \Delta t \int_{\Gamma_3^p} N_a N_b s_b^{r+1} d\Gamma \qquad (2.11)$$

where Δt is the time step size, r denotes the current time step and $r+1$ indicates the new step. Prescribed boundary fluxes are given at the nodal points.

Discretization of equation (2.8) follows the same steps as the discretization of equation (2.4), and the first weak form reads

$$\int_{\Omega^c} \frac{\kappa_p^{r+1}}{\mu} \frac{dN_a}{dx} \frac{dN_b}{dx} p_b^{r+1} d\Omega = -\int_{\Omega^c} N_a N_b s_b^{r+1} d\Omega \,. \qquad (2.12)$$

where the equivalent intrinsic permeability κ_p (m^3) has a scalar value that is given by $\kappa_p = a^3/12$ in a 2D flow domain and $\kappa_p = a^3 \mathrm{b}/12$ if the line element is imbedded in a 3D domain.

The condition of limit equilibrium for a horizontally oriented erosion channel is evaluated at the integration points and is given in a two-dimensional flow domain by

$$\kappa_p^{r+1} = \tfrac{1}{12}\left(a^{r+1}\right)^3, \quad a^{r+1} \frac{dN_b}{dx} p_b^{r+1} = \frac{\pi}{3}\left(\rho^s - \rho^l\right) g d_{70} \eta \tan\vartheta \,. \qquad (2.13)$$

The sink term in equation (2.12), where s is positive for flow out of the channel, provides a source term in equation (2.11), where s is positive for flow into the subsurface, and vice versa. Linear one-dimensional elements are used for solving equation (2.12), whereas linear triangular elements discretize equation (2.11) in case of a two-dimensional flow domain and tetrahedral elements are used for resolving a three-dimensional problem. Combining both equations yields

$$\int_{\Omega^p} N_a N_b \left(\alpha + n\beta\right) S^{r+1} \left(p_b^{r+1} - p_b^r\right) d\Omega + \int_{\Omega^p} N_a N_b n \left(\frac{dS}{dp}\right)^{r+1} \left(p_b^{r+1} - p_b^r\right) d\Omega =$$

$$-\Delta t \int_{\Omega^p} \frac{k_r^{r+1} \kappa_{ij}}{\mu} \frac{\partial N_a}{\partial x_i} \frac{\partial N_b}{\partial x_j} p_b^{r+1} d\Omega + \Delta t \int_{\Omega^p} \frac{k_r^{r+1} \kappa_{ij}}{\mu} \frac{\partial N_a}{\partial x_i} \rho^l g_j d\Omega$$

$$-\Delta t \int_{\Gamma_3^p} \frac{\kappa_p^{r+1}}{\mu} \frac{\partial N_a}{\partial x_i} \frac{\partial N_b}{\partial x_j} p_b^{r+1} d\Omega + \Delta t \int_{\Gamma_2^p} N_a N_b \bar{q}_b^{r+1} \qquad (2.14)$$

The interface elements align along the horizontal axis. Picard iteration over κ_r^{r+1} and S^{r+1} are used to resolve the non-linearities in the system of equations. Nonlinearities in κ_p^{r+1} are resolved sequentially. For a given trial channel height, equation (2.13) provides the equivalent intrinsic permeability, which is attached to the relevant interface element. The product of channel height and pressure gradient that follows from the solution of equation (2.14) is then compared with the equilibrium condition given by the right hand side of expression (2.15).

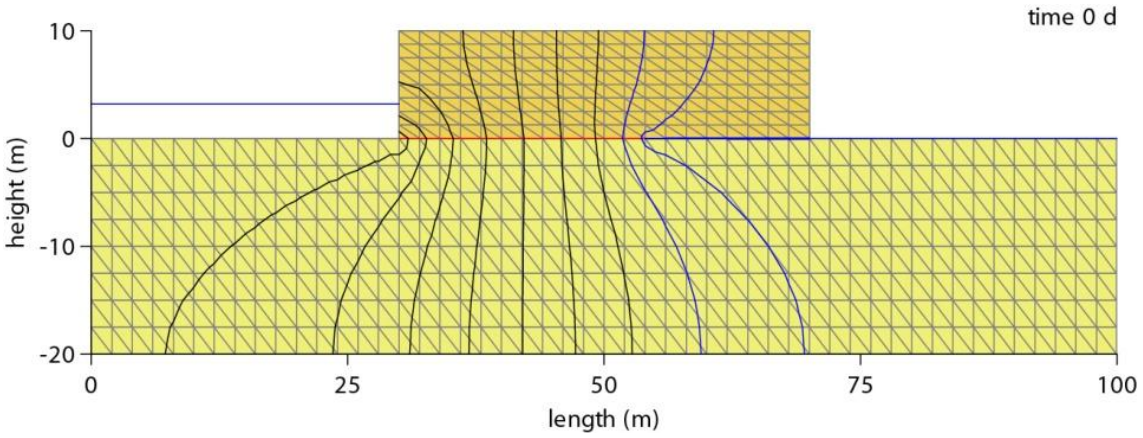

Figure 2.2 Simplified dam geometry

Figure 2.2 shows the layout of a sample problem that includes a simplified dam geometry with a low permeable structure that is supported by an aquifer of high permeability, as well as the finite element mesh used for the flow simulation. To the left side of the structure the river water level imposes a hydraulic head condition on the horizontal edge of the aquifer and to the right side of the structure a constant polder water level applies. The vertical boundaries and base of the aquifer are considered impervious as well as external dam boundaries. The structure itself has a low permeability, hardly supporting groundwater flow.

Thus, water flows under the structure through the aquifer from the river side towards the polder. Sellmeijer (1988) considered an impermeable structure on top of an aquifer with the same hydraulic loading conditions.

Figure 2.2 shows the result of a steady state computation where the piping channel did not reach the upstream side yet and the channel remains stable for the imposed head difference. The channel is captured by interface elements located at predefined position under the dam. Current inactive interface elements are colored red and active interface elements that support Poiseuille flow through the channel are colored blue. The flow direction is normal to the equipotential lines as the permeability tensor is isotropic. The active 15 meter long piping channel that drains the aquifer to some extent, causes a shift in the otherwise symmetrically arranged equipotential lines as shown.

Figure 2.3 provides the sequential procedure for resolving the non-linearity in the interface permeability graphically for two interface elements of the sample problem that are in series. The height of the channel is presented as a function of hydraulic head gradient. Hydraulic head $h\,(\mathrm{m})$ is presented as $h = p/(\rho^{l} g) + y$, where $y\,(\mathrm{m})$ is the elevation level. The dark blue line represents the limit equilibrium condition; below this line stable grain conditions apply and above the equilibrium line unstable conditions hold.

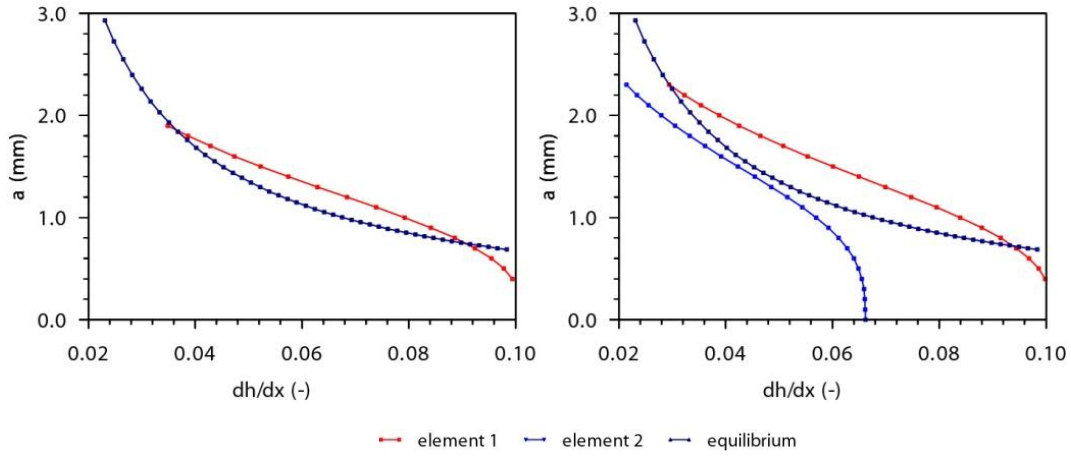

Figure 2.3 Activation algorithm

The calculation process starts by checking the interface element located to the downstream side of the channel (element 1) next to the exit point. For a thickness of 0 mm the head gradient is determined by the flow process through the subsurface. Increasing the thickness of the element increases the effective permeability of the element and decreases the gradient over the element leading to the red line in Figure 2.3 (a).

The height of the channel is increased stepwise until the condition becomes unstable. This unstable situation is associated with the first (right) point where the red line intersects the equilibrium line. At this point the element becomes active for the given head difference over the structure; a small increase in the channel height pushes the element in the unstable zone. The permeability of the element is increased until the element becomes stable again. The element thickness for which equilibrium holds is obtained by means of a bisection algorithm. This second (left) intersection point denotes a stable situation. If the height of the channel increases above this point, the element enters the stable zone.

The procedure continues by checking the element on the upstream side (element 2) of the first element (element 1). The plot on the right of Figure 2.3 illustrates this process. The height is increased sequentially until the line enters the unstable zone and the second intersection point is found, or as this example show a threshold value for the maximum channel height has been reached within the stable zone indicating that the element will not be activated. For the depicted situation, the applied head difference over the structure will not activate the second element. During the process the height of the already activated elements is modified accordingly until equilibrium is satisfied within the entire pipe domain.

Figure 2.3 shows that the occurrence of piping can be predicted using two processes: primary erosion at the tip of the channel and secondary erosion along the bottom of the channel. Primary erosion is also related to initiation phase of piping, whereas both types of erosion play a part in the equilibrium phase and progressive phase of the pipe as was explained by Van Beek et al. (2015). The first part of the path that the interface element follows in the stable zone until the height of the element intersects the equilibrium condition has to be explained by the primary erosion process, the second part of the path in the instable zone corresponds to the secondary erosion process of piping. The equilibrium line in Figure 2.3 captures the secondary erosion process. The head gradient required to start the secondary erosion process (primary erosion) is larger than the head gradient at equilibrium conditions. This is in agreement with the observations made by Van Beek and Bezuijen (2012a). In this report the primary erosion criterion is either set to

$$\frac{\partial p}{\partial x} \geq c \quad or\ to \quad a_{tip} \geq 3d_c \tag{2.15}$$

3 Sand box experiments

The experimental work by Hanses (1985) offered valuable information with respect to the influence of set up dimensions on the critical head. However, limited experimental work has been performed on the influence of sand characteristics on critical head and pipe hydraulics. Therefore additional experimental work has been performed by Van Beek ea. (2014a) to investigate the influence of the sand type on the critical head for pipe progression. Several experiments allowed for the investigation of pipe dimensions, pipe hydraulics and erosion mechanism as well. The outcome of these laboratory experiments were used to validate the piping module of DgFlow (Van Esch ea., 2013a).

3.1 Laboratory tests

Figure 3.1 shows the experimental setup Van Beek ea. (2014a) constructed in the laboratory. In the experiments the confined sand sample is subjected to a head drop, thereby simulating the flow of water through an aquifer beneath an impermeable water-retaining structure. At the upstream side, the sand sample is contained by a filter. The top plate in the experiments is transparent and is coated with silicone gel on the inside, to obtain a somewhat rough surface that resembles a clay cover. A circular exit hole is created in the cover for the exit of water. The exit hole in the covering glass plate simulates the case where a confining upper layer is locally punctured such that flow from the aquifer concentrates towards one point. The high flow velocity near the exit will ensure pipe initiation at a relatively low head drop, allowing the process of pipe progression to be investigated. A cylinder is submerged in the plate, connected to the outlet, to allow for the deposition of sand around the hole. Three types of experiments are performed, denoted as small-scale experiments, medium-scale experiments and visualization experiments. This report considers the small-scale experiments. The dimensions (length, width, height) of the contained sample in the small-scale experiments are respectively 0.48x0.30x0.105 m, with a seepage length of 0.343 m. The exit hole diameter is 6 mm and its height (representing the thickness of the confining layer) is 5 mm. Its height is dimensioned small compared to the dimensions of the box, 5 mm (5% of the sand sample depth), in order to keep exit head losses as low as possible. This in contrast to the height of the exit in the experiments by Hanses (1985), which equals approximately the sand sample depth and resulted in considerable exit losses for some experiments.

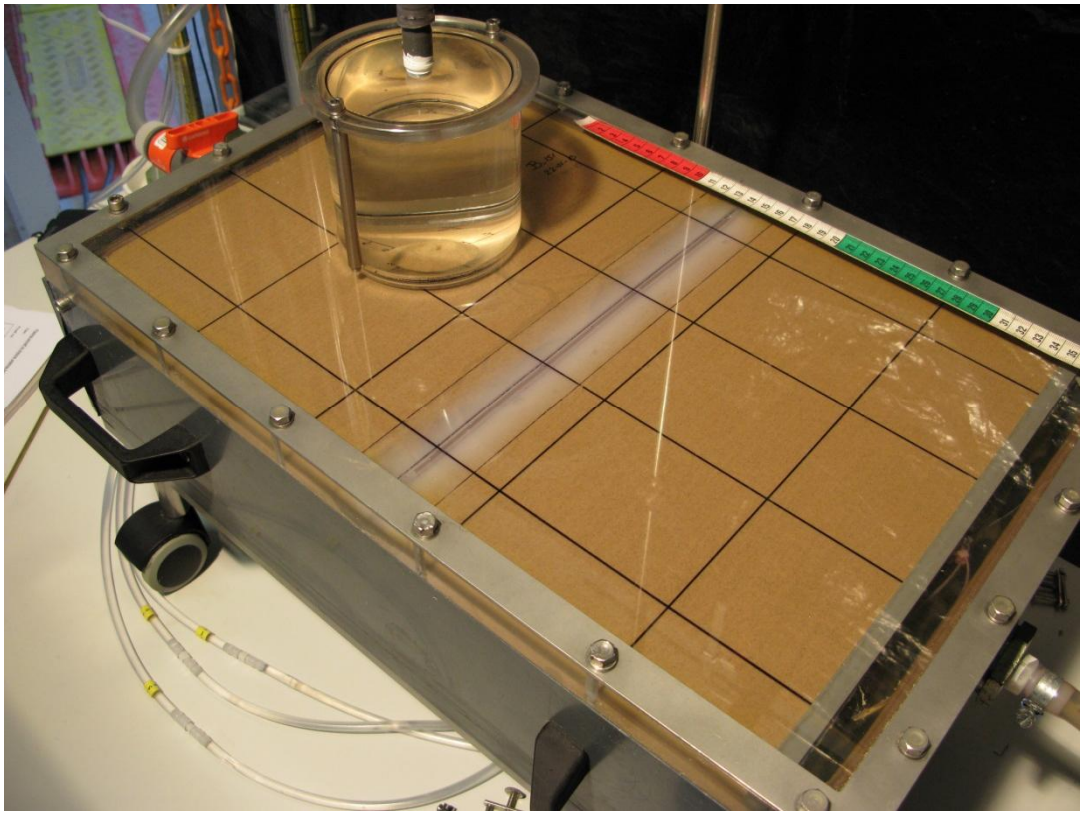

Figure 3.1 Laboratory setup

The potential is measured using riser tubes, placed at various locations in the sand sample. The potential measurements allow for estimation of the permeability and the upstream filter resistance.

The sand sample is rained into the box while in upright position (inlet facing downward). Dense samples (relative density >85%) are prepared by raining dry sand in de-aired water, during continuous tamping. Loose to medium-dense samples are prepared by raining dry sand in de-aired water, such that a loose sample is obtained that is densified to the required density by applying a pulse.

The tests are performed by stepwise increasing the hydraulic head at the inflow side until erosion takes place. If sand transport is observed, increase of head is delayed until the erosion process is stabilized in which no sand is transported in or near the pipes and the flow and heads observed in the riser tubes are constant.

In total 19 small-scale experiments were performed. Table 3.1 gives an overview of the sand characteristics and critical heads of the small scale experiments that were selected for model validation.

Here number and code label the experiment, K, RD, R, H_e, W_t and W_m denote hydraulic conductivity, relative density, hole diameter, experimentally obtained critical head, pipe width at the tip and mean pipe width. The letter in the experiment code indicates the sand type: B for baskarp, W for Waalre, O for Oostelijk rivierzand, I for Itterbeck and E or Enschede sand. All sands are sieved to remove the fine fraction. Two mixtures have been created by adding fines to a sieved fraction. In the small-scale experiments, the relative density and exit hole diameter have been varied as well. The resulting critical heads show that the reproducibility of the small-scale experiments is particularly good for the experiments on Baskarp sand and reasonable for the other experiments.

The pipe tip width is determined for four lengths in the small-scale experiments. The pipe tip width is relatively constant upon lengthening, but is often larger for the pipe length at ¾ of the seepage length, than for the other analyzed lengths. Possibly, the critical pipe length has been exceeded at this point, such that the water pressures at the tip of the pipe are relatively large, causing a larger area to be involved in the erosion process (Van Beek, 2014a).

Figure 3.2 to Figure 3.5 show the evolution of piping channels for experiment B133.

Nr	Code	d70 (mm)	K (m/s)	RD (-)	R (mm)	H_{exp} (m)	W_t (mm)	W_m (mm)
1	B115	0.154	$5.4 \cdot 10^{-5}$	0.89	6	0.080	1.83	n.a.
2	B118	0.154	$6.3 \cdot 10^{-5}$	0.89	6	0.080	1.71	3.06
3	W131	0.400	$5.4 \cdot 10^{-4}$	0.65	6	0.086	9.57	15.30
4	B133	0.154	$9.5 \cdot 10^{-5}$	0.65	6	0.065	3.60	7.67
5	O140	0.307	$2.0 \cdot 10^{-4}$	0.65	6	0.095	9.88	11.20
6	B142	0.154	$6.2 \cdot 10^{-5}$	0.91	6	0.080	4.06	9.37
7	B143	0.154	$5.5 \cdot 10^{-5}$	0.91	12	0.084	4.67	6.42
8	B144	0.154	$5.3 \cdot 10^{-5}$	0.91	12	0.085	4.19	9.02
9	B145	0.154	$8.0 \cdot 10^{-5}$	0.65	12	0.069	4.29	8.42
10	B146	0.154	$8.0 \cdot 10^{-5}$	0.65	12	0.070	4.32	6.82
11	O163	0.307	$1.3 \cdot 10^{-4}$	0.94	6	0.185	7.14	25.02
12	I164	0.278	$1.3 \cdot 10^{-4}$	0.97	6	0.113	5.56	7.88
13	I166	0.223	$4.6 \cdot 10^{-5}$	1.00	6	0.210	5.28	22.17
14	I167	0.203	$3.7 \cdot 10^{-5}$	0.93	6	0.152	4.99	10.16
15	I168	0.203	$2.7 \cdot 10^{-5}$	0.89	6	0.205	4.97	9.47
16	E169	0.431	$3.2 \cdot 10^{-4}$	0.94	6	0.090	10.98	15.55

Table 3.1 Small scale test: width 0.3 m, height 0.1 m, length 0.48 m, hole at 0.344 m

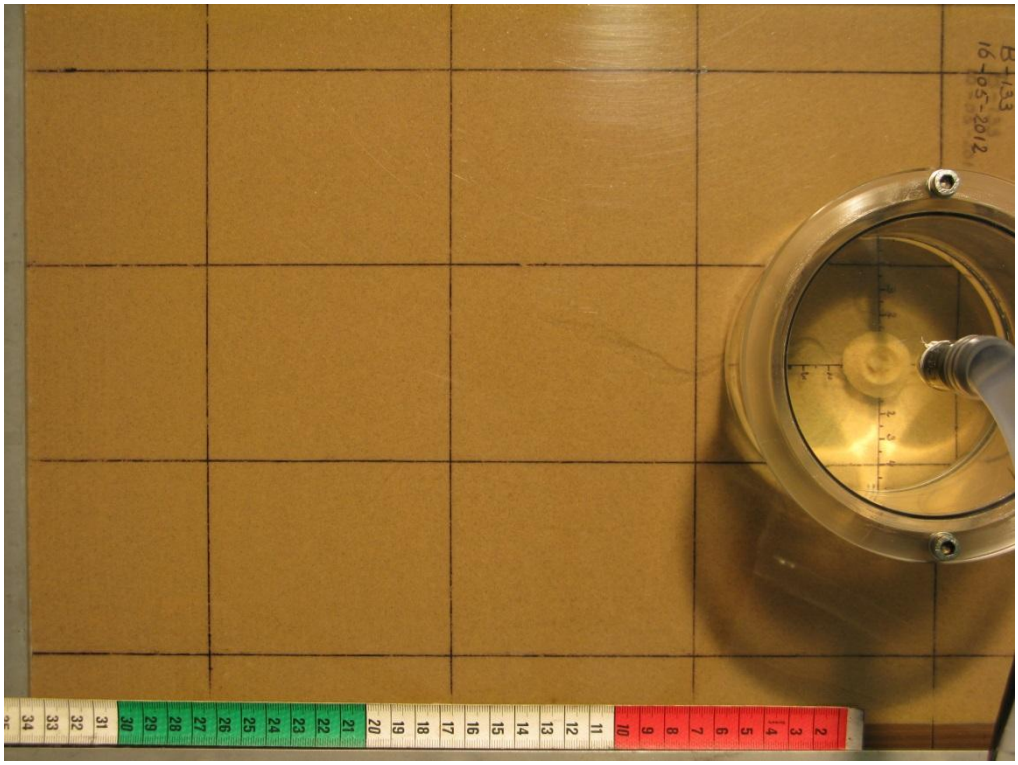

Figure 3.2 Experiment B133, H = 0.050 m.

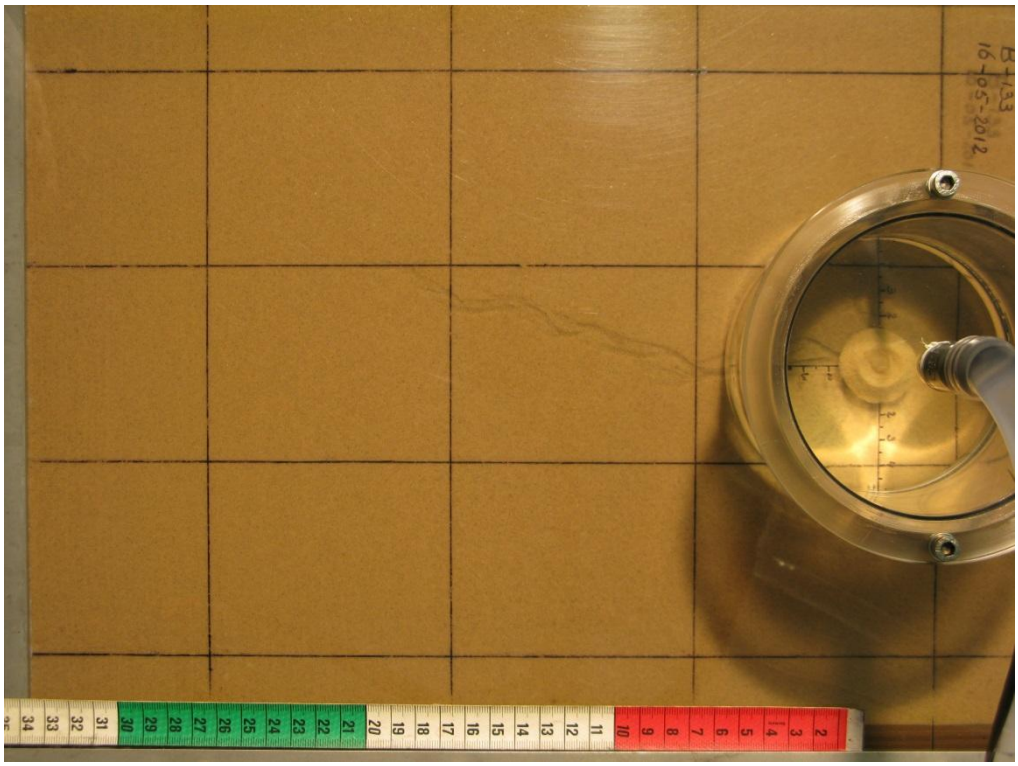

Figure 3.3 Experiment B133, H = 0.055 m.

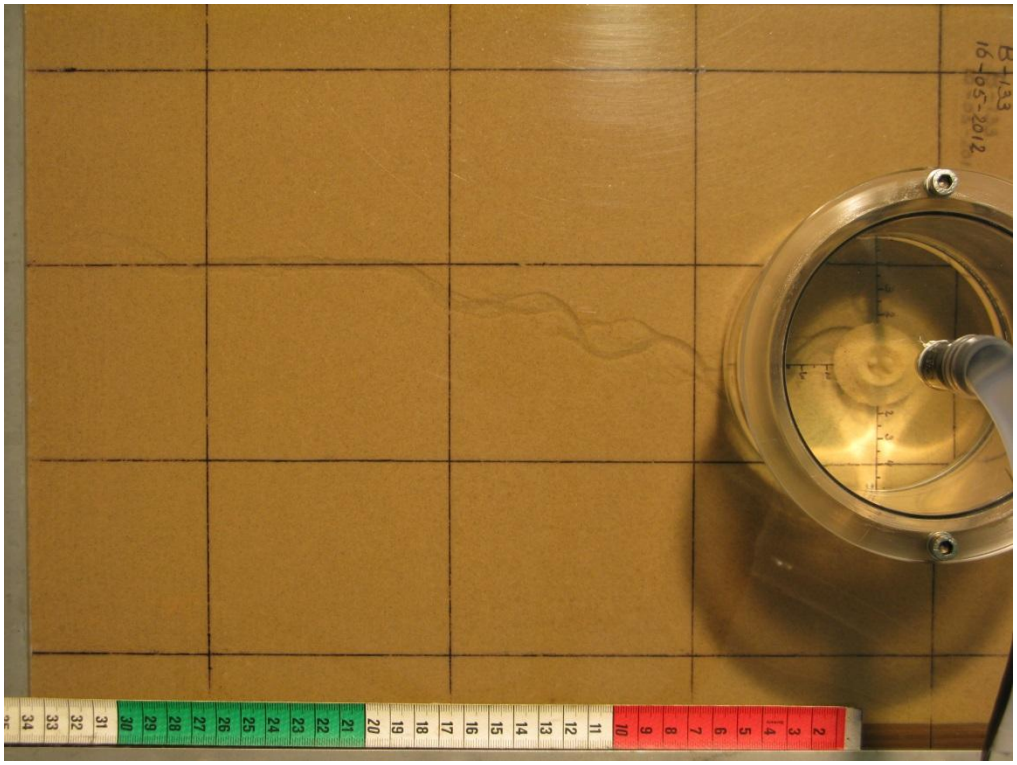

Figure 3.4 Experiment B133, H = 0.065 m.

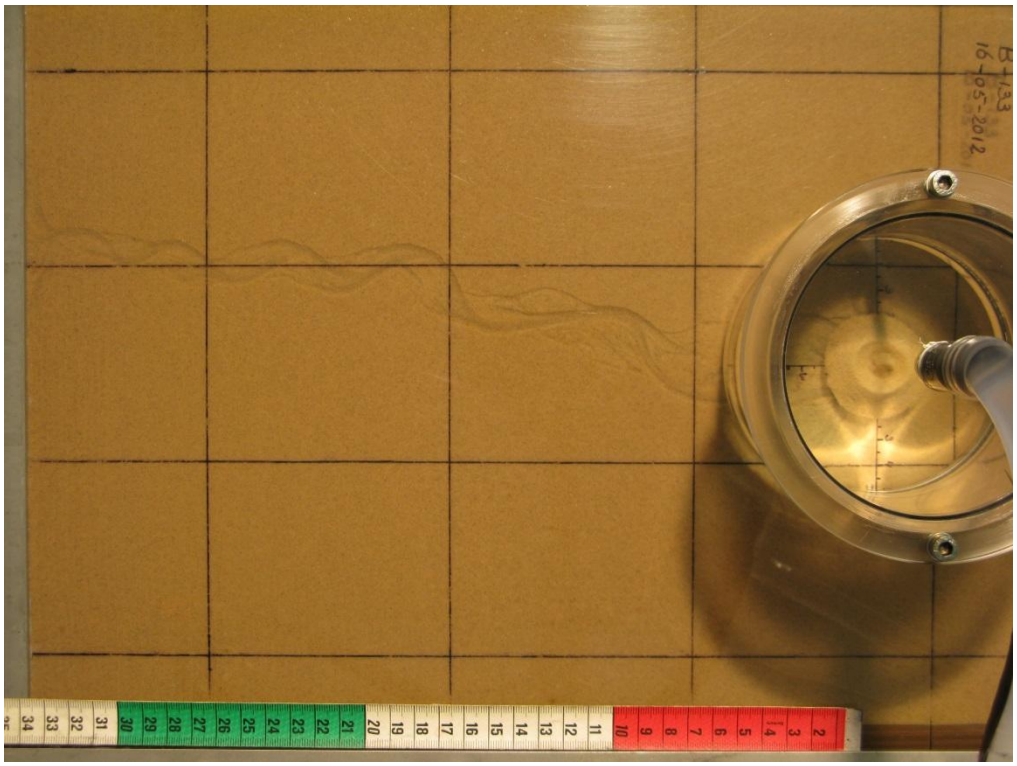

Figure 3.5 Experiment B133, H = 0.065 m.

3.2 Model verification

This section compares the outcome of Sellmeijer's rule with results of two-dimensional DgFlow simulations for the lab experiment that were presented previously. The two-dimensional flow conditions were obtained by imposing multiple piping elements on top of the three-dimensional sand box. DgFlow calculations with a single piping channel, for which the width of the channel was set to the width of the sandbox, give a quasi-three dimensional solution. The comparison of two-dimensional DgFlow calculations and quasi-three dimensional computations indicates the effect of including the third dimension in the flow simulation.

Sellmeijer's rule

At present the most advanced design rule for piping is the rule proposed by Sellmeijer ea. (2011). This rule is based on the analysis of pipes under an impervious structure of base length L (m) on top of a single aquifer of constant height D (m). Sellmeijer's rule predicts the critical head difference H_c (m) between the outer river water level at one side of a structure and the polder water level to the other side of the structure. If the actual head difference is larger than the critical head difference, a piping channel will propagate until the channel reaches the upstream side. The rule in its current form is given by

$$H_c = F_r F_s F_g L, \tag{3.1}$$

where F_r (-) expresses the resistance term, F_s (-) denotes the scaling term, and F_g (-) expresses the geometry term, in which

$$F_r = \frac{\rho^s - \rho^l}{\rho^l}\eta \tan\vartheta, \quad F_s = \frac{d_{70}}{\sqrt[3]{\kappa L}}, \quad F_g = 0.91\left(\frac{D}{L}\right)^{\varsigma}, \quad \varsigma = \frac{0.24}{\left(\frac{D}{L}\right)^{2.8} - 1}. \tag{3.2}$$

In the expression of the resistance term ρ^s $(\mathrm{kg/m^3})$ corresponds to the density of the soil particles, ρ^l $(\mathrm{kg/m^3})$ denotes the density of the water phase, η (-) expresses White's constant, and ϑ (deg) is the bedding angle. The scaling term includes the intrinsic permeability κ $(\mathrm{m^2})$ of the sand under the structure, the grain diameter d_{70} (m) and the potential piping length. The geometric term relates the thickness of the aquifer to the potential piping length and includes a coefficient 0.91, which was determined using numerical

modeling. According to Sellmeijer's rule larger values of L, ρ^s, η, ϑ, d_{70}, and smaller values for D, κ and ρ^l increase the critical head difference H_c and reduce the risk of piping.

Two-dimensional DgFlow model

This section discusses the verification of DgFlow against Sellmeijer's rule. Figure 3.6 to Figure 3.11 show the experimental setup for the verification tests. The model simulates flow through a sandbox and the development of 21 piping channels at the top. This number of piping channels corresponds to the number of 3D elements in y-direction of the experiment, which generates a 2D flow situation if the width of the pipes is set to the sandbox width divided by 20 except for the pipes at the boundary; their width corresponds to the experiment width divided by 40. The pictures show surfaces with a constant pressure and velocity vectors that visualize the flow through the porous material to an outlet strip at the top surface. In time the hydraulic head was increased at the left vertical boundary, the remaining parts of the boundary (except for the outlet strip) are no-flow boundaries.

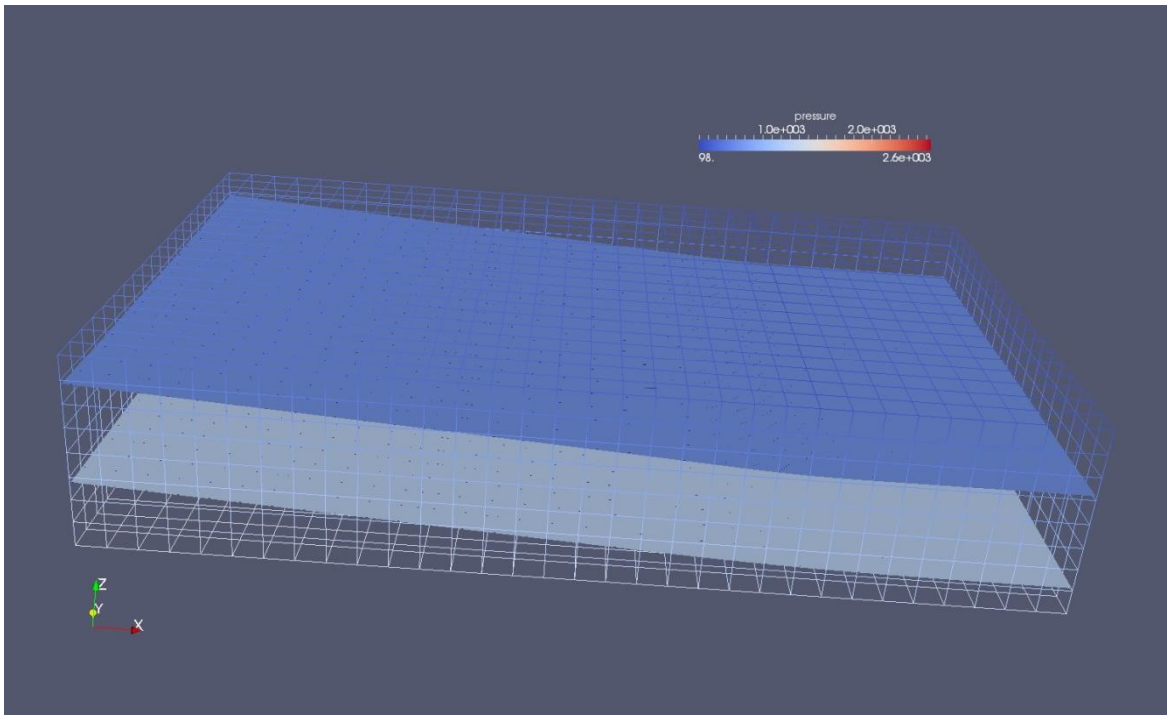

Figure 3.6 Verification setup stage 1

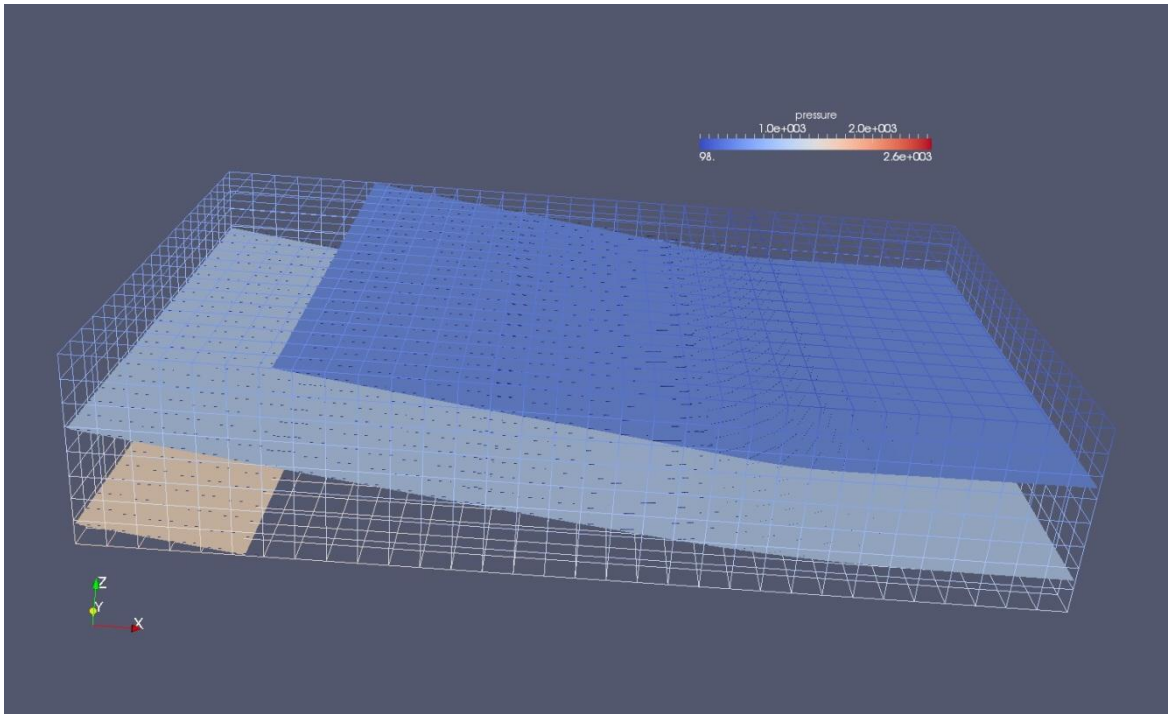

Figure 3.7 Verification setup stage 2

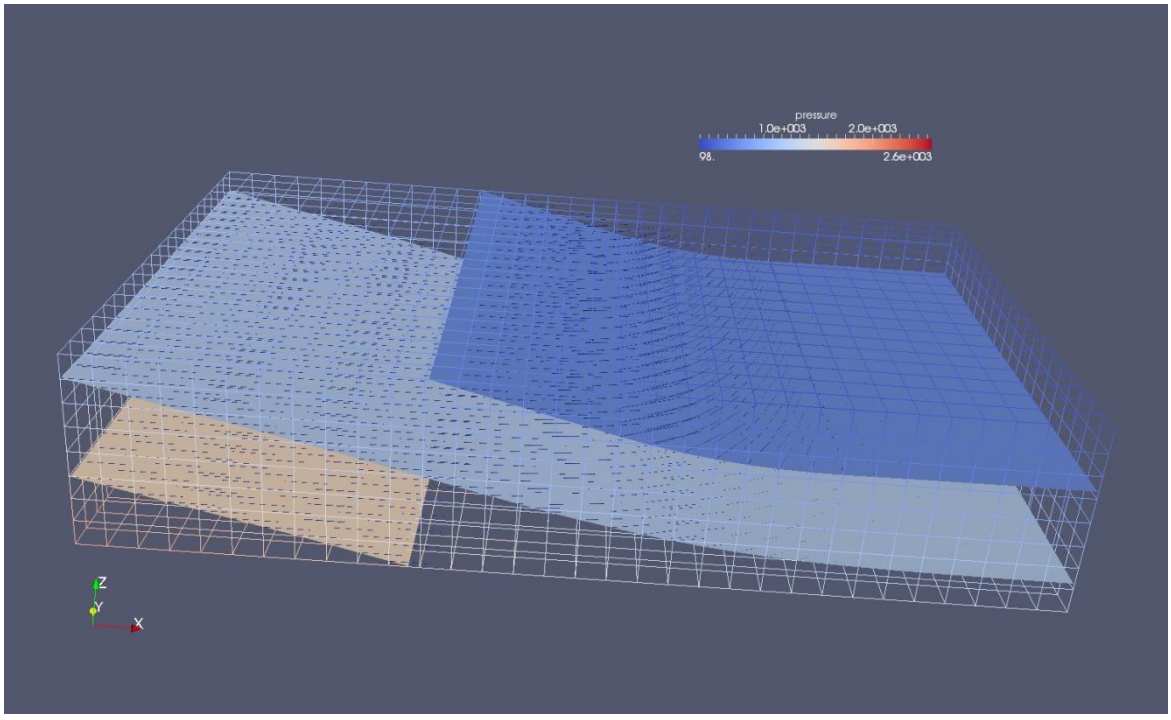

Figure 3.8 Verification setup stage 3

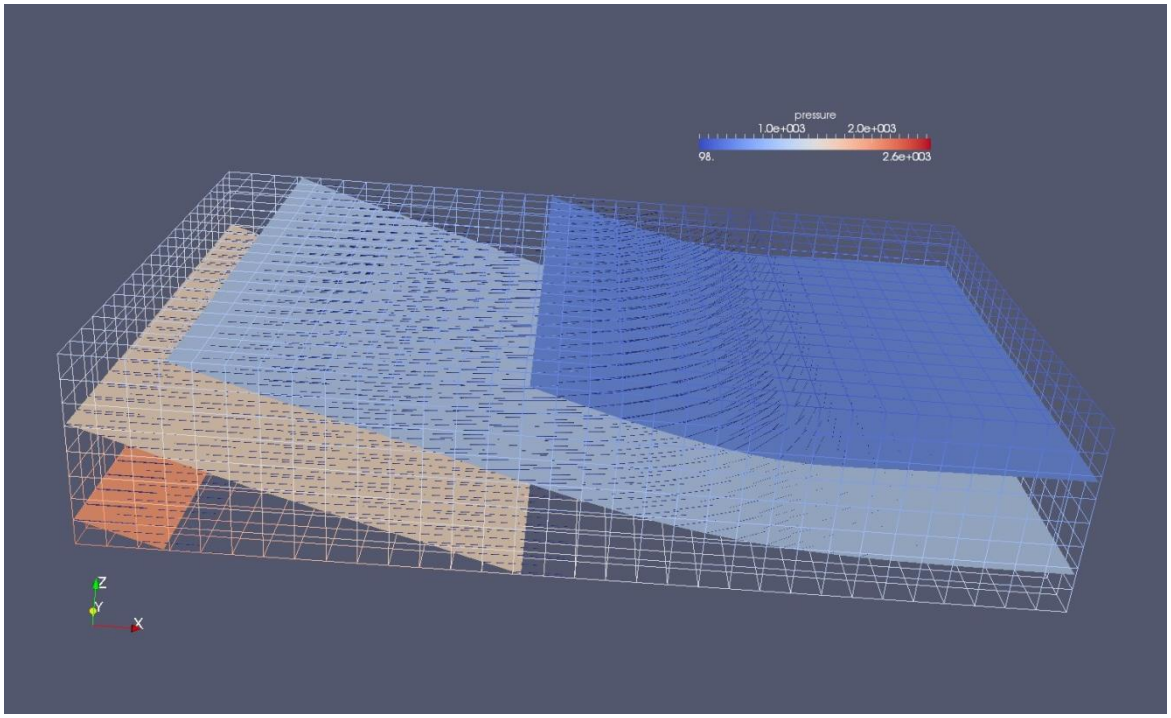

Figure 3.9 Verification setup stage 4

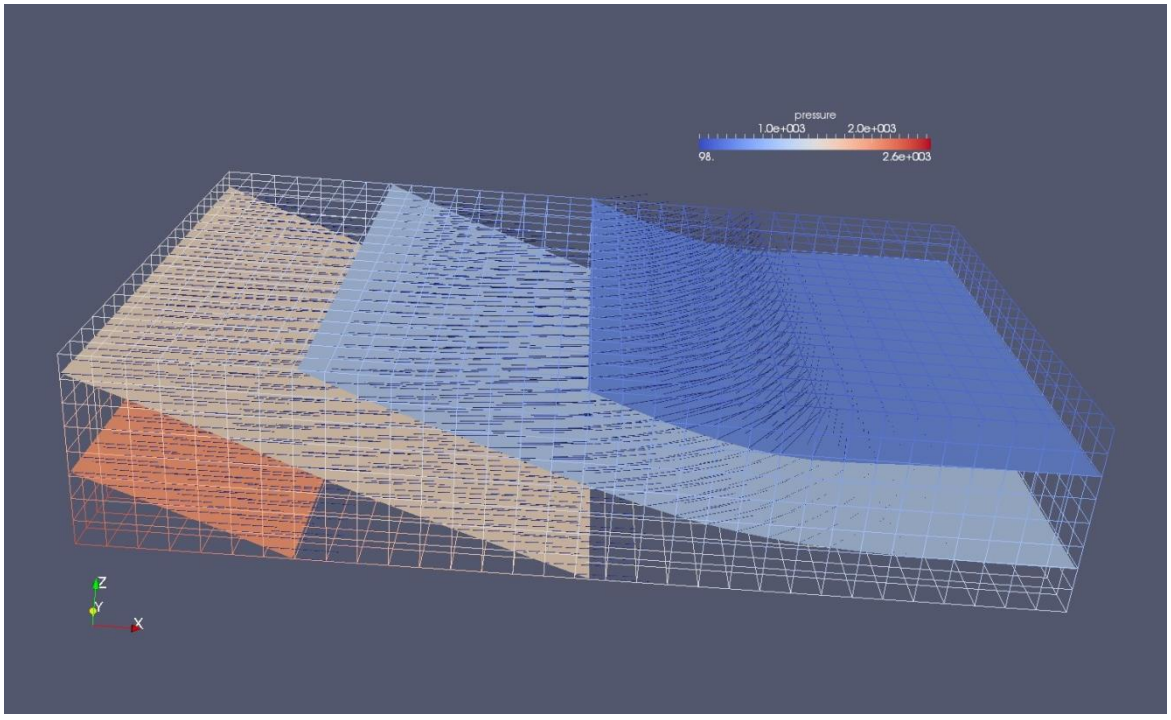

Figure 3.10 Verification setup stage 5

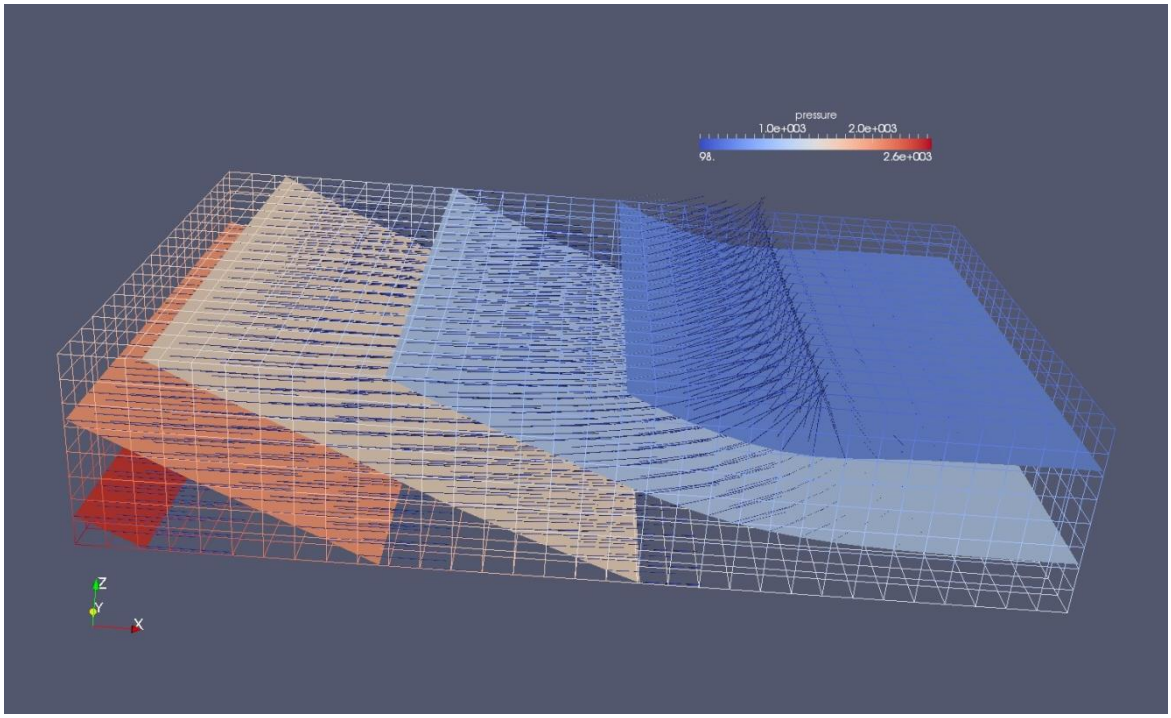

Figure 3.11 Verification setup stage 6

Quasi three-dimensional DgFlow model

Figure 3.12 to Figure 3.17 show the setup of a quasi-three dimensional computation. At the start of the simulation hydrostatic pressures apply. Figure 3.12 shows this situation and depicts a single horizontal pressure plane. Figure 3.13 shows the next stage of the simulation where the hydrostatic head at the left boundary is increased, pressure planes get slightly tilted and the arrows indicate that that water leaves the sandbox through the hole in the covering impermeable plate. Figure 3.14 shows an increase in fluid velocities and the development of a small pipe. The arrows indicate flow from the underlaying sand layer into the pipe, from which the flow rate to the pipe and the flow out of the domain was calculated under grain equilibrium conditions. The flow velocities in the pipe itself are not shown grapihically. The length of the pipe increases even further in stage 4 and 5 as depicted in Figure 3.15 and Figure 3.16 where the channel reached the upstream side of the flow domain. Figure 3.17 shows the final stage where the head was increased even further but the channel remained to have its maximum channel height as the model is not able to simulate the widening process.

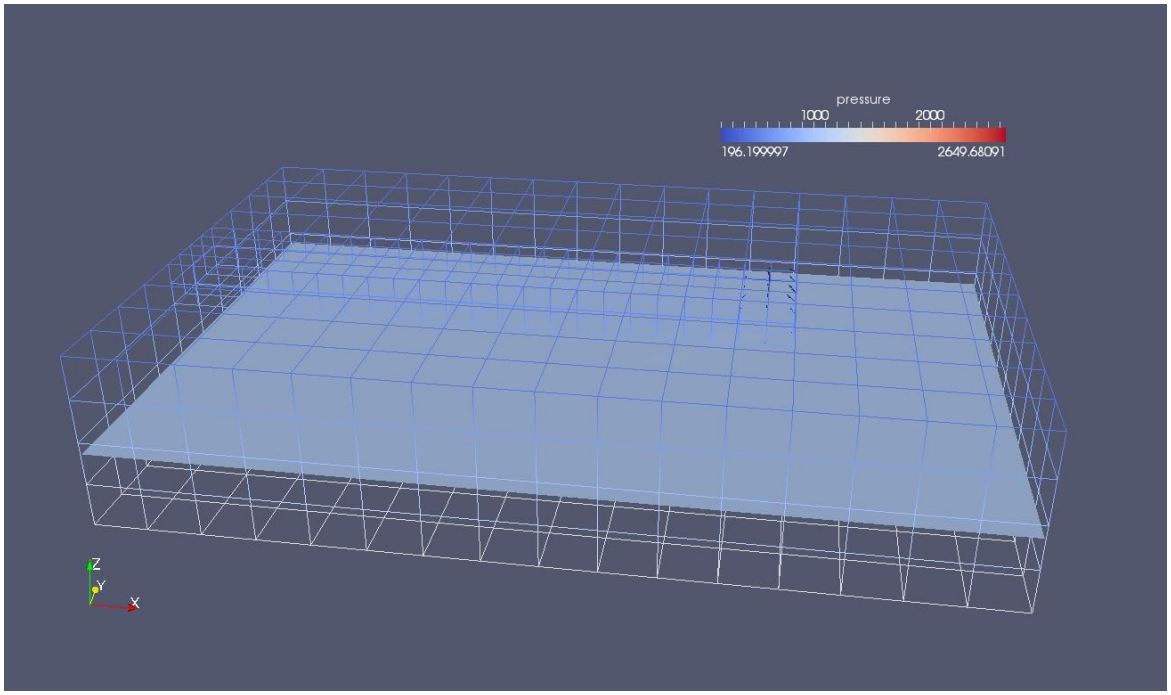

Figure 3.12 Validation setup stage 1

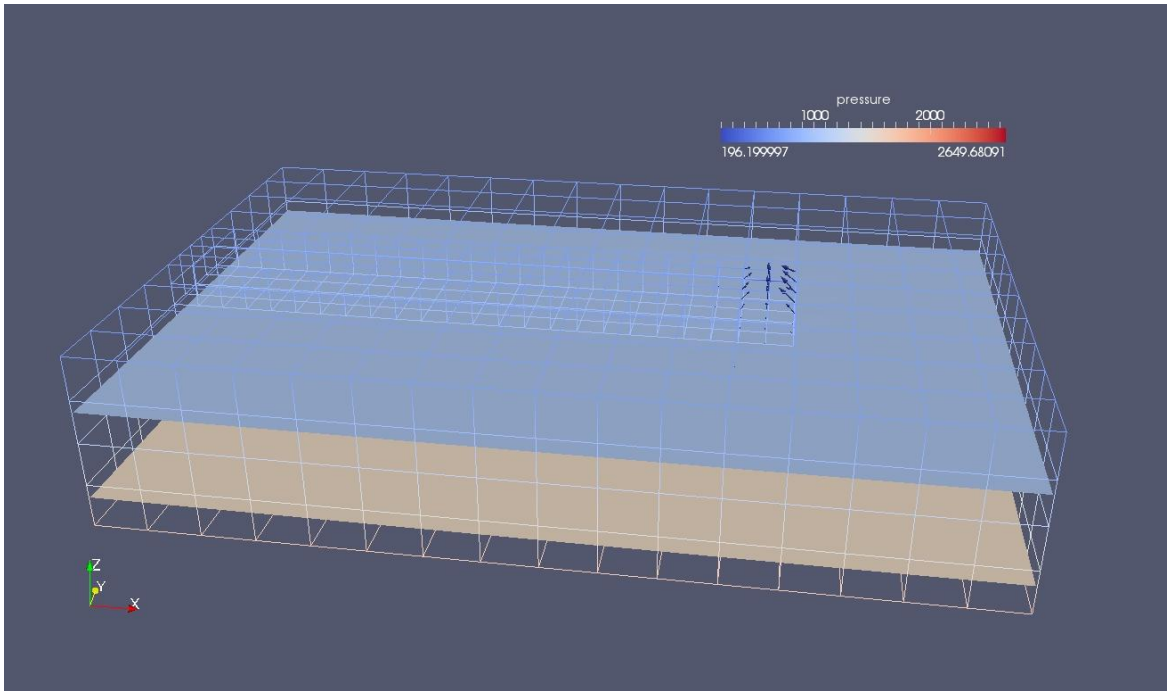

Figure 3.13 Validation setup stage 2

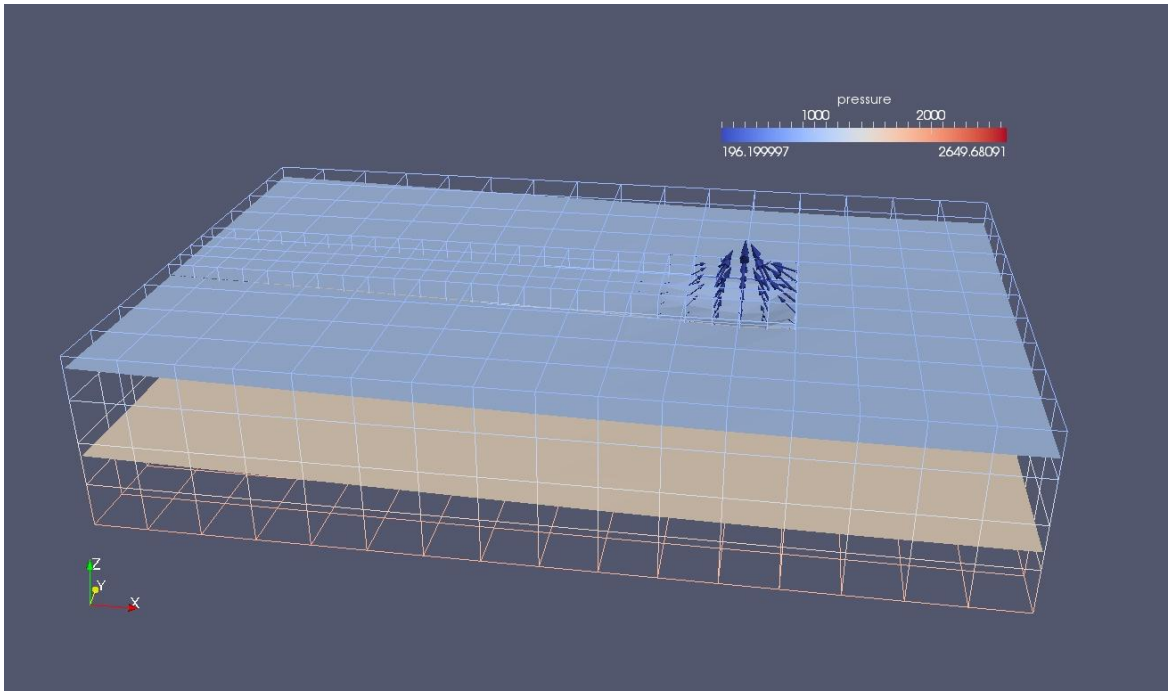

Figure 3.14 Validation setup stage 3

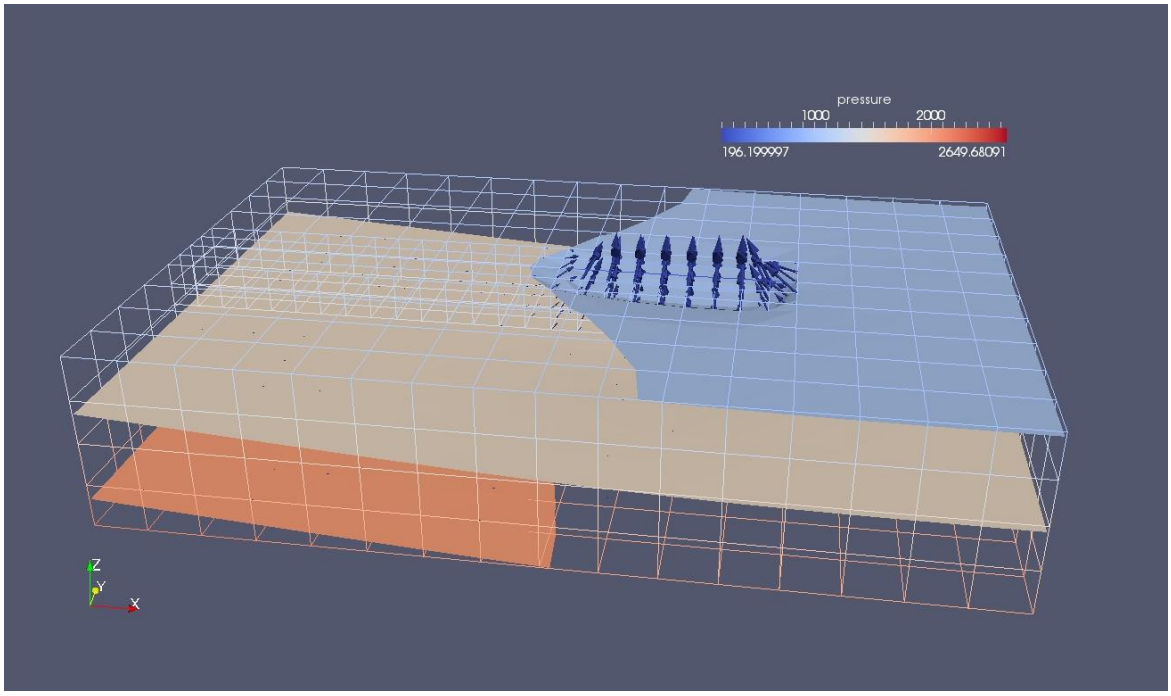

Figure 3.15 Validation setup stage 4

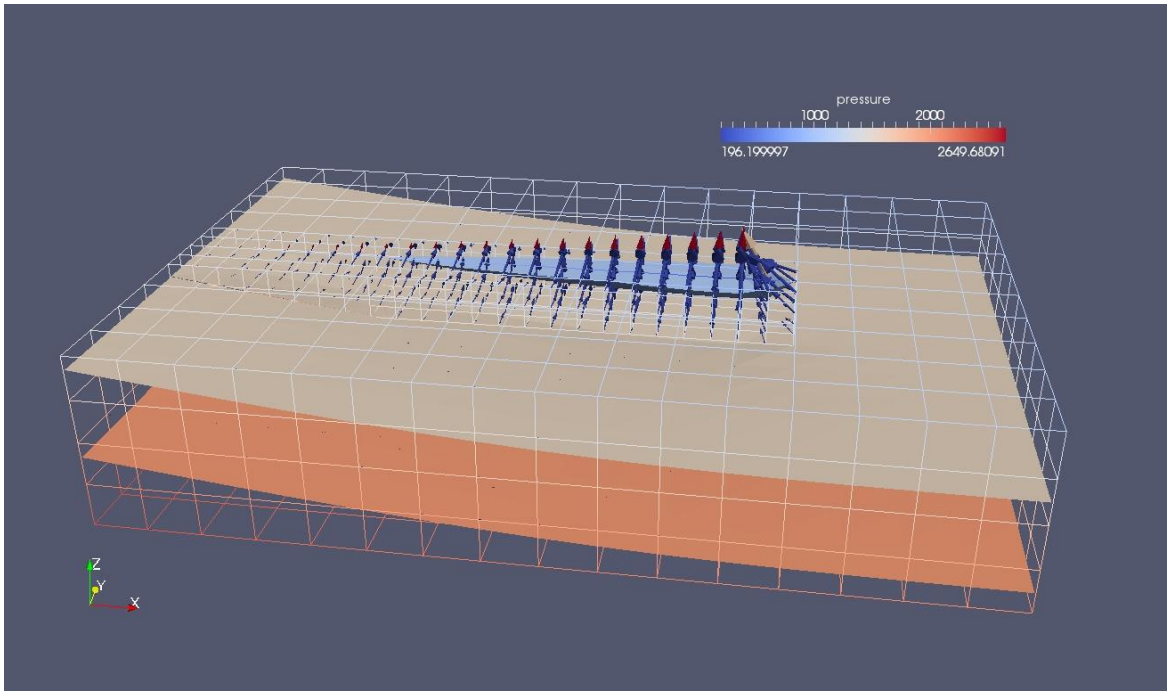

Figure 3.16 Validation setup stage 5

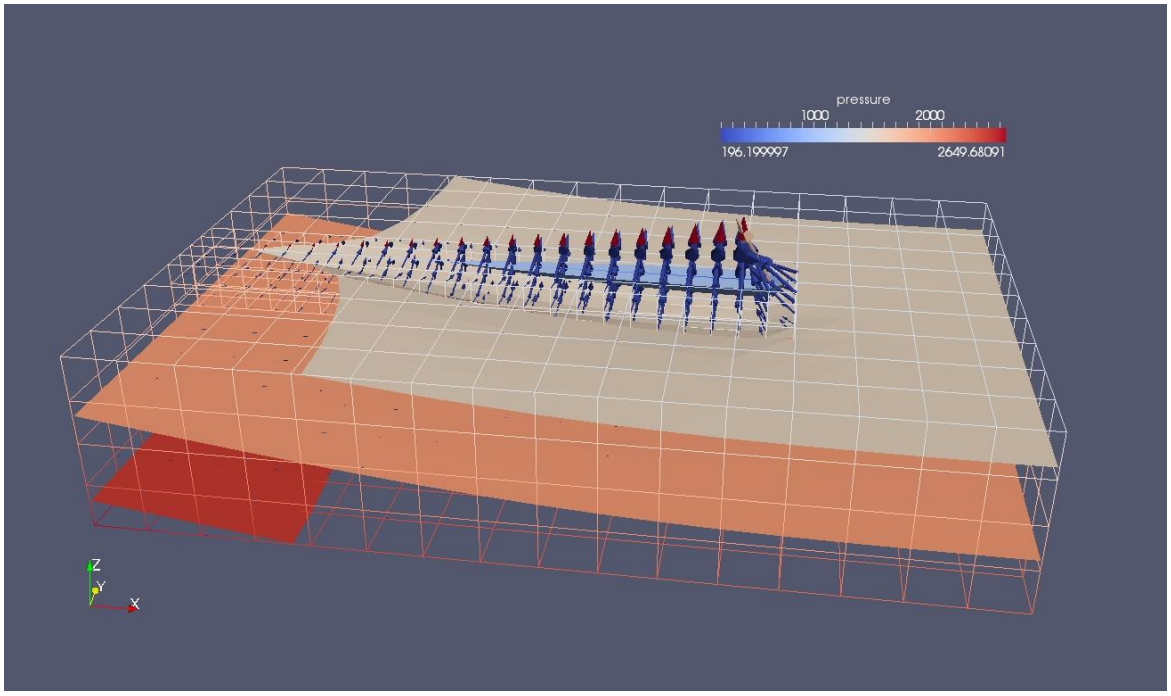

Figure 3.17 Validation setup stage 6

Comparison of the results

Table 3.2 compares the outcome of Sellmeijer's rule (H_{sel}) with the observed critical heads (H_e) for 17 laboratory experiments and relates the outcome of a two-dimensional DgFlow situation ($H_{multiple}$), which was modeled by imposing multiple piping channels in the three-

dimensional sand box to the quasi-three dimensional DgFlow simulation that imposed a single channel. The table shows a good match between the outcome of Sellmeijer's rule and the DgFlow algorithm. The table also indicates that the computed heads are approximately twice as large as the experimentally observed heads. In the quasi three-dimensional flow simulation, the flux through the pipe was scaled with the box width. The results show that a three dimensional computation results in critical heads that are significantly lower than two dimensional calculations. Setting the width of the channel to a more realistic (smaller) value supports a fully three-dimensional computation and reduces the critical heads even further. Figure 3.18 shows the critical head per experiment and presents the comparison graphically. Figure 3.19 presents the predicted critical heads relative to the measured critical heads per experiment.

Nr	Exp. Code	H_{exp} (m)	H_{sell} (m)	$H_{multiple}$ (m)	H_{single} (m)
1	B115	0.080	0.165	0.160	0.064
2	B118	0.080	0.157	0.152	0.064
3	W131	0.086	0.200	0.198	0.077
4	B133	0.065	0.137	0.137	0.052
5	O140	0.095	0.213	0.219	0.086
6	B142	0.080	0.158	0.152	0.064
7	B143	0.084	0.163	0.160	0.067
8	B144	0.085	0.165	0.161	0.068
9	B145	0.069	0.144	0.145	0.052
10	B146	0.070	0.144	0.147	0.056
11	O163	0.185	0.246	0.259	0.093
12	I164	0.113	0.223	0.226	0.090
13	I166	0.210	0.253	0.252	0.105
14	I167	0.152	0.248	0.258	0.091
15	I168	0.205	0.275	0.267	0.103
16	E169	0.090	0.256	0.252	0.108

Table 3.2 Sellmeijer's results for the small scale experiment

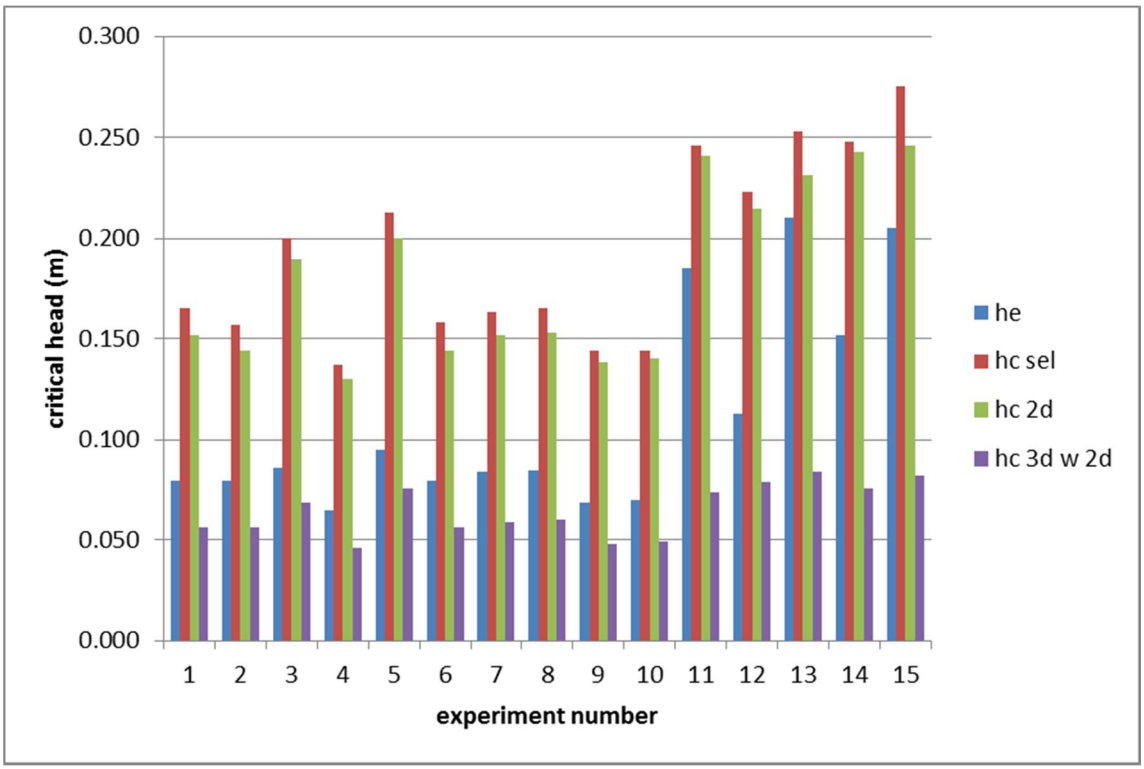

Figure 3.18 Experimental results versus Sellmeijer, DgFlow 2D and DgFlow quasi 3D

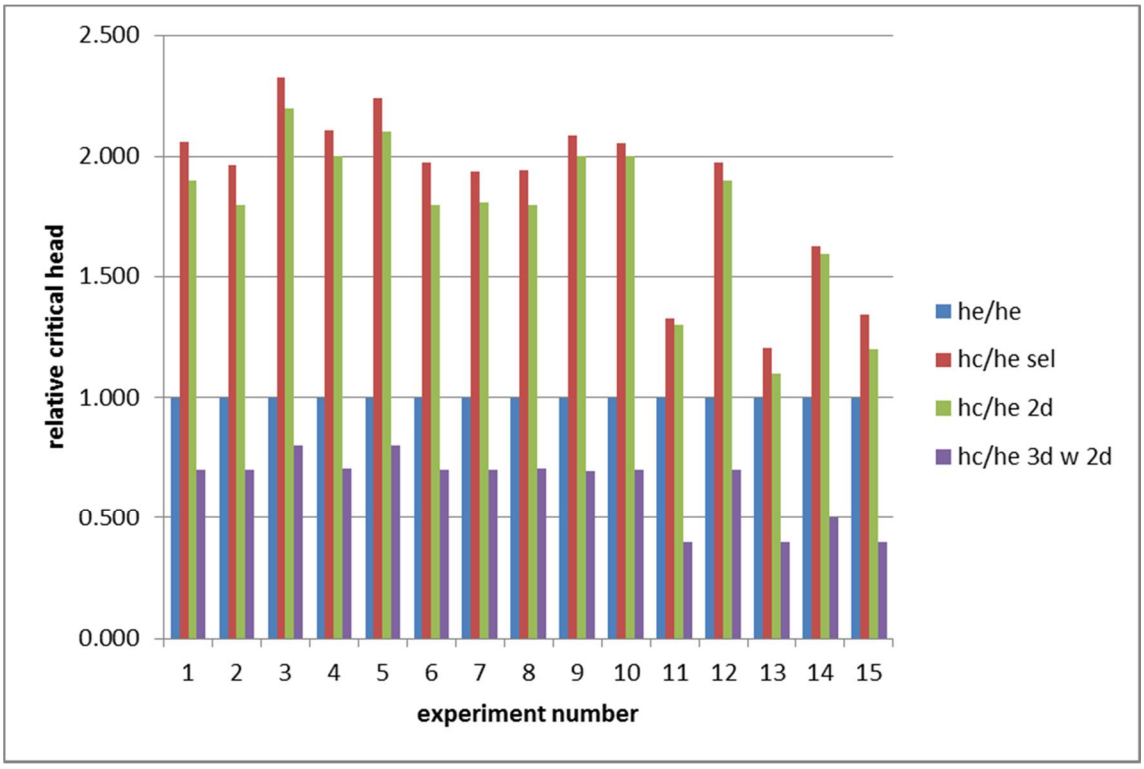

Figure 3.19 Sellmeijer, DgFlow 2D and DgFlow quasi relative to experimental results.

3.3 Model validation

Model validation focuses on: numerical aspects, parameter sensitivity and the mathematical description of the physical process that are contribute to the piping mechanism. Van Esch (2014) reported on these aspects and this report checks the accuracy of DgFlow predictions in relation to the mesh size, investigates the width of the piping channel related to the height of the pipe and adds a formulation for the primary erosion process to the model.

Numerical aspects

In order to investigate the numerical aspects three finite element meshes are constructed: a coarse scale, a medium scale and a fine scale mesh, for which the outcome will be compared. The coarse scale discretisation applies 16 x 10 x 4 elements, which generates elements with a dimension of 0.030 x 0.030 x 0.025 meters as the small scale experiments had a dimension of 0.48 x 0.30 x 0.10 meters. The coarse scale discretization reduces the total number of elements to 640 and the number of nodes to 935. The medium scale discretisation applies 32 x 20 x 8 elements, which generates 5120 elements with a dimension of 0.015 x 0.015 x 0.0125 meters and 6237 nodes. The fine scale discretisation applies 64 x 20 x 8 elements, which generates 10240 elements with a dimension of 0.0075 x 0.015 x 0.0125 meters and 12285 nodes.

Appendix A presents the geometrical information on the position of the pipe for each experiment on a fine scale mesh. All further calculations, exept for the mesh dependency study presented here, where made on the fine grid. The top picture shows the finite element mesh and the piping channel as it was observed in the laboratory experiment. The picture below shows the height of the pipe along the pipe track for the critical situation that starts the progressive phase.

Table 3.3 gathers the critical heads predicted by DgFlow simulations and the experimentally obtained values for the critical heads. Figure 3.20 shows the calculated critical head next to its measured value per experiment and Figure 3.21 presents the critical head relative to the experimentally obtained values.

	Sand box experiment			Numerical simulations		
nr	Code	w (mm)	H_{exp} (m)	H_{coarse} (m)	H_{medium} (m)	H_{fine} (m)
1	B115	n.a.	0.080	0.033	0.033	0.034
2	B118	3.06	0.080	0.034	0.038	0.038
3	W131	15.30	0.086	0.094	0.095	0.109
4	B133	7.67	0.065	0.042	0.047	0.048
5	O140	11.20	0.095	0.083	0.085	0.088
6	B142	9.37	0.080	0.053	0.056	0.055
7	B143	6.42	0.084	0.052	0.051	0.06
8	B144	9.02	0.085	0.057	0.055	0.054
9	B145	8.42	0.069	0.049	0.053	0.054
10	B146	6.82	0.070	0.044	0.050	0.052
11	0163	25.02	0.185	0.136	0.141	0.151
12	I164	7.88	0.113	0.062	0.072	0.076
13	I166	22.17	0.210	0.128	0.132	0.142
14	I167	10.16	0.152	0.106	0.111	0.108
15	I168	9.47	0.205	0.096	0.098	0.106
16	E169	15.55	0.090	0.110	0.113	0.113

Table 3.3 Critical head 3D DgFlow simulations and measured heads

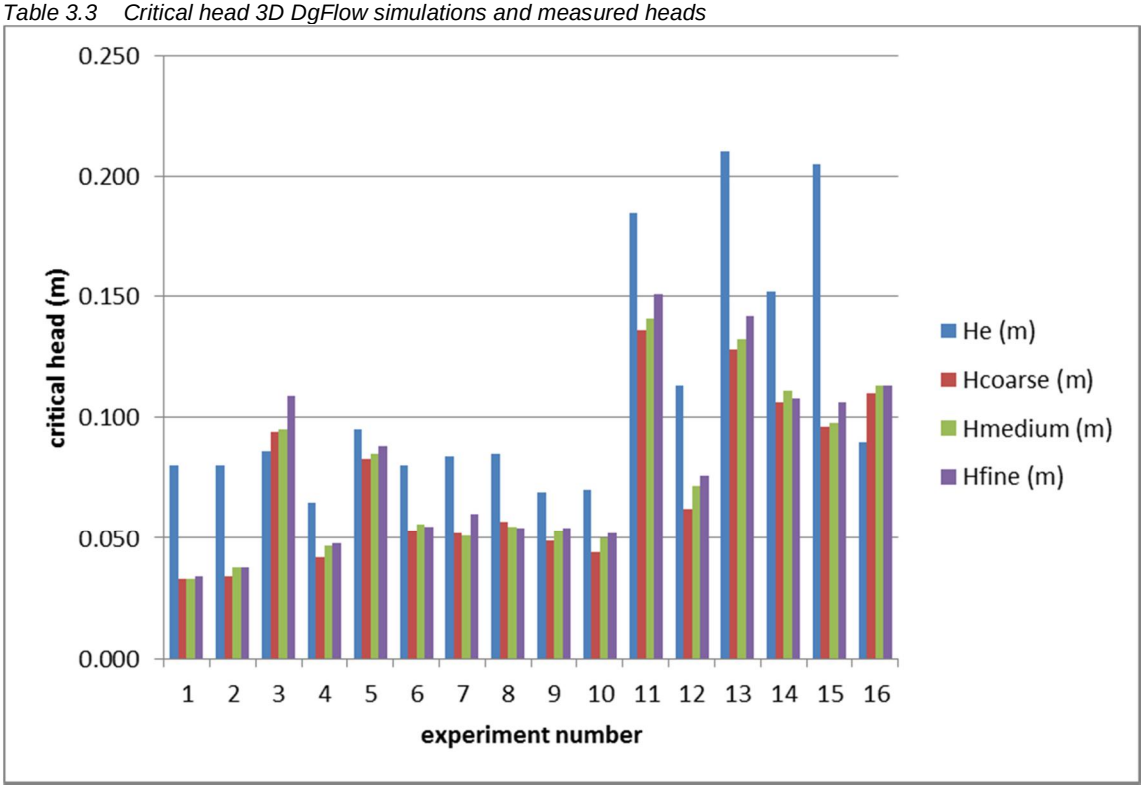

Figure 3.20 Critical head 3D DgFlow simulations versus measured heads.

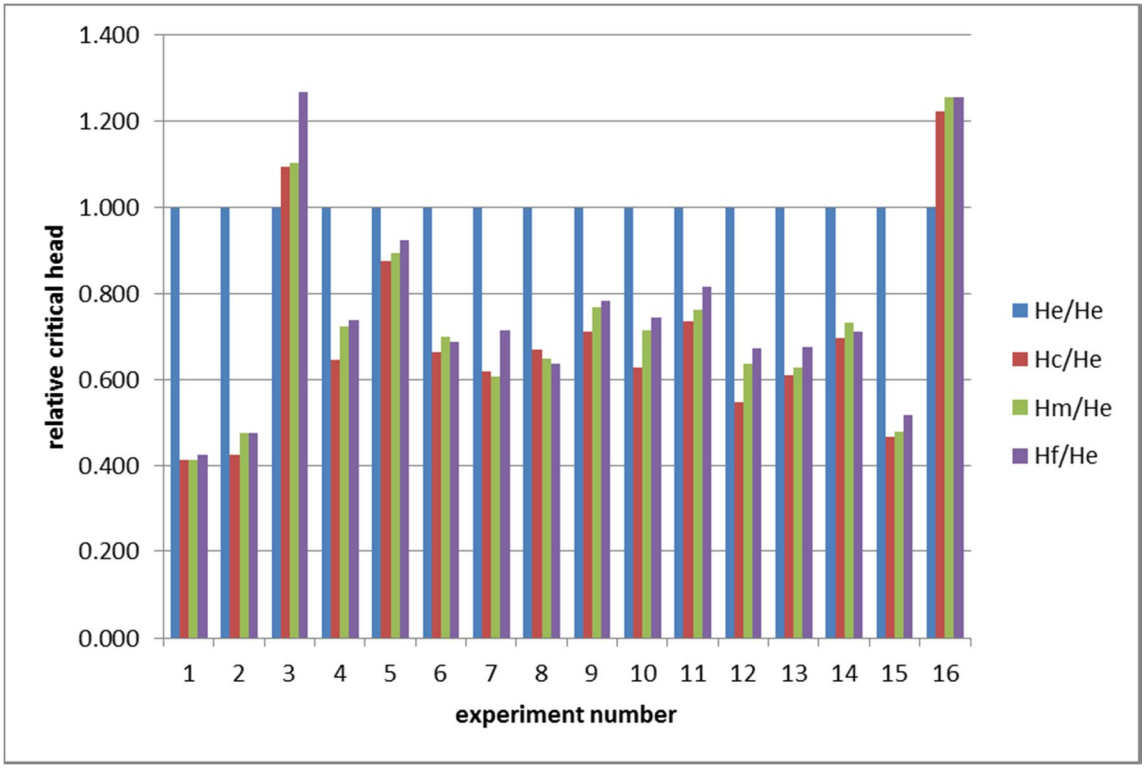

Figure 3.21 Critical head 3D DgFlow simulations relative to measured heads.

Apart from laboratory test W131 and E169 all numerical results show a lower value of the critical head. It must be noted that the bedding angle was set to 37^{o}, which followed from calibration studies in the past and applied to piping through a slit. If the bedding angle is increased to 48^{o} then the critical heads increase by a factor 1.5, which gives a better match for most of the tests.

Pipe width formulation

Table 3.4 gathers the results for the calibrated pipe width and mean pipe height that follows from DgFlow computations. Figure 3.22 shows the critical head for mean and calibrated pipe width versus measured heads and Figure 3.23 presents the critical head for mean and calibrated pipe width relative to measured critical heads. Figure 3.24 plots the calibrated pipe height versus pipe width.

	Sand box experiment			Numerical simulation		
nr	Code	w (mm)	H_c(m)	w (mm)	h (mm)	H_c(m)
1	B115	n.a.	0.080	23.8	0.270	0.080
2	B118	3.06	0.080	28.6	0.345	0.083
3	W131	15.30	0.086	7.51	0.963	0.086
4	B133	7.67	0.065	19.0	0.457	0.066
5	O140	11.20	0.095	14.1	0.742	0.094
6	B142	9.37	0.080	28.8	0.289	0.080
7	B143	6.42	0.084	17.6	0.420	0.085
8	B144	9.02	0.085	35.2	0.244	0.087
9	B145	8.42	0.069	17.6	0.466	0.070
10	B146	6.82	0.070	16.6	0.483	0.069
11	0163	25.02	0.185	46.0	0.458	0.181
12	I164	7.88	0.113	25.9	0.487	0.114
13	I166	22.17	0.210	71.7	0.229	0.183
14	I167	10.16	0.152	28.3	0.247	0.150
15	I168	9.47	0.205	68.5	0.210	0.188
16	E169	15.55	0.090	7.86	0.913	0.091

Table 3.4 Calibrated pipe width and corresponding pipe height.

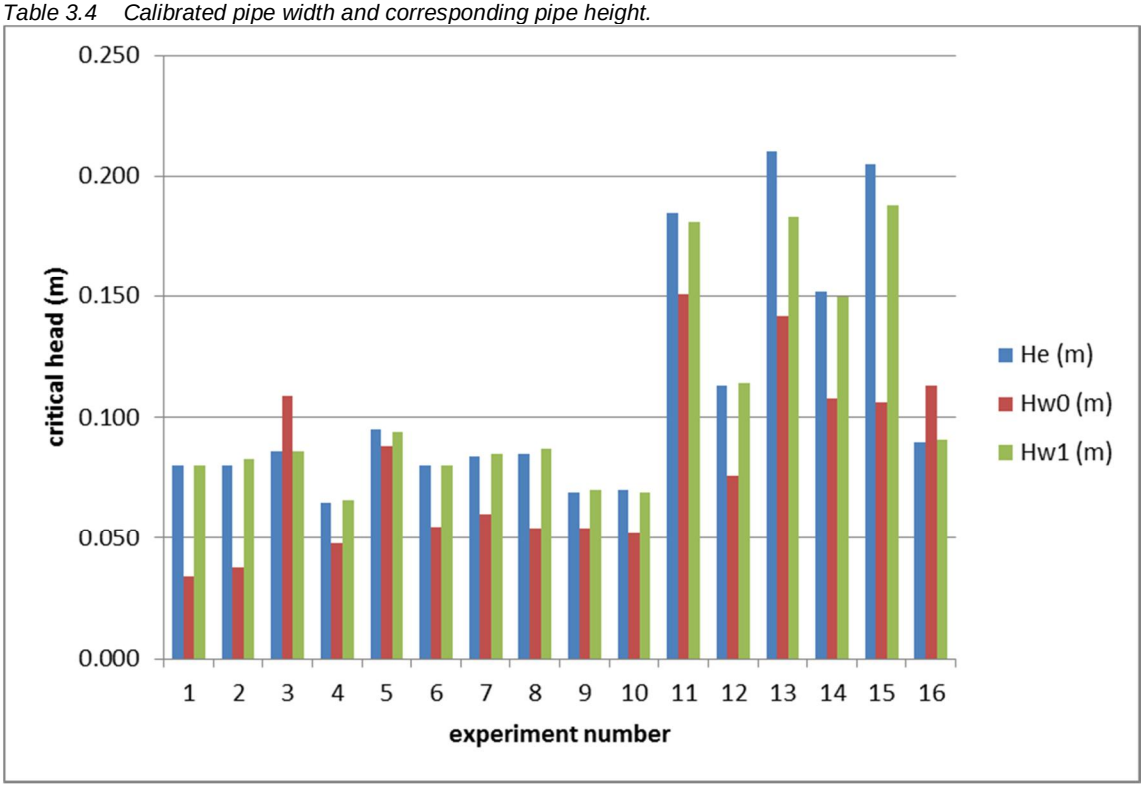

Figure 3.22 Critical head for mean and calibrated pipe width versus measured heads.

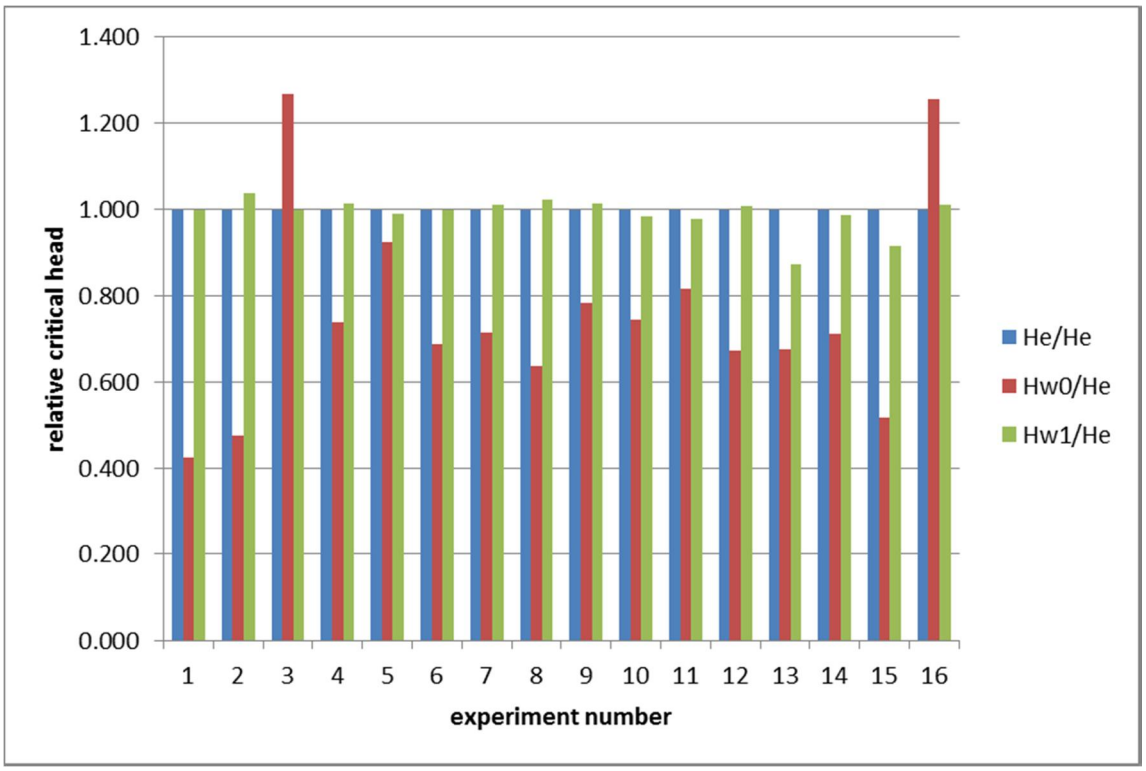

Figure 3.23 Critical head for mean and calibrated pipe width relative to measured heads.

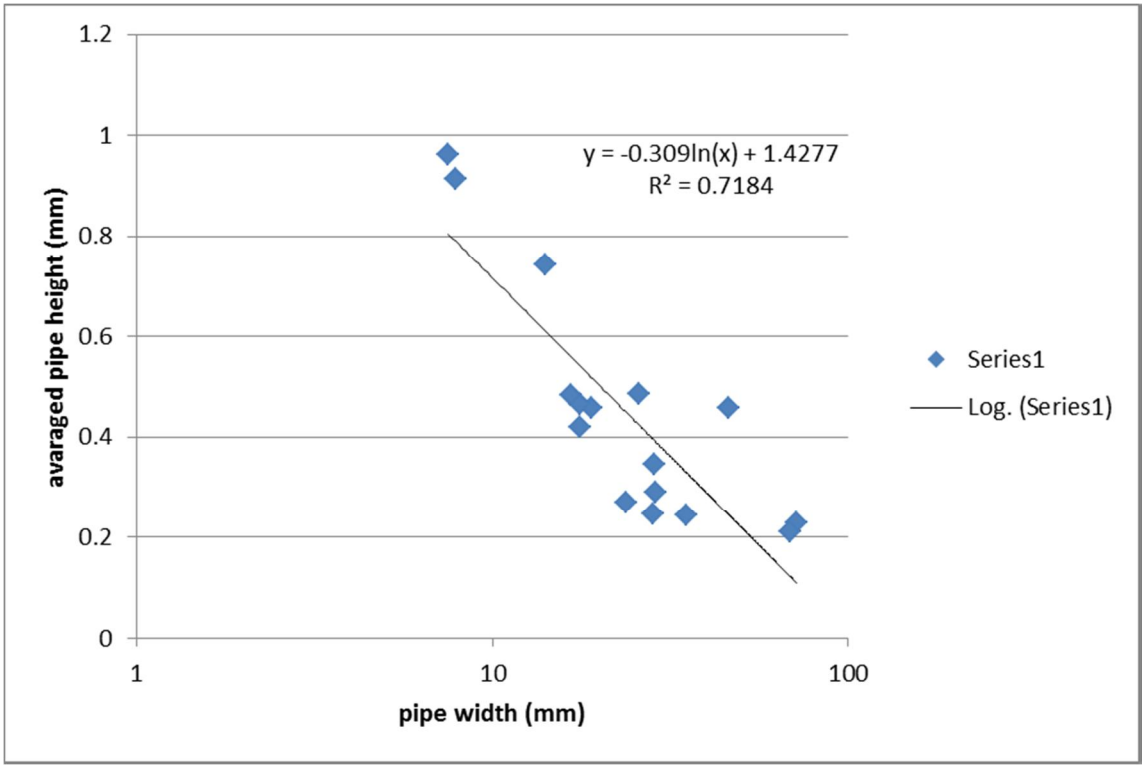

Figure 3.24 Calibrated pipe height versus pipe width.

Bedding angle calibration

Table 3.5 gathers the results for the calibrated pipe width and mean pipe height that follows from DgFlow computations. The calibrated bedding angles required for the calculated gradient to match the results of the measured gradients are high. This does not necessarily mean that the bedding angles are incorrect, but can also point towards a width that is incorrect. Figure 3.25 shows the critical head for mean and calibrated pipe width versus measured heads and Figure 3.26 presents the critical head for mean and calibrated pipe width relative to measured heads.

Sand box experiment			**Numerical simulations**			
nr	Code	H_c(m)	ϑ_1 (deg)	H_{c1}(m)	ϑ_2 (deg)	H_{c2}(m)
1	B115	0.080	37	0.034	60.58	0.080
2	B118	0.080	37	0.038	57.77	0.080
3	W131	0.086	37	0.109	30.73	0.086
4	B133	0.065	37	0.048	45.58	0.065
5	O140	0.095	37	0.088	39.13	0.095
6	B142	0.080	37	0.055	47.62	0.079
7	B143	0.084	37	0.06	46.53	0.083
8	B144	0.085	37	0.054	49.87	0.087
9	B145	0.069	37	0.054	43.92	0.068
10	B146	0.070	37	0.052	45.41	0.069
11	0163	0.185	37	0.151	42.71	0.184
12	I164	0.113	37	0.076	48.25	0.113
13	I166	0.210	37	0.142	48.10	0.211
14	I167	0.152	37	0.108	46.68	0.151
15	I168	0.205	37	0.106	55.54	0.205
16	E169	0.090	37	0.113	30.97	0.090

Table 3.5 Critical head 3D DgFlow simulations bedding angle calibration.

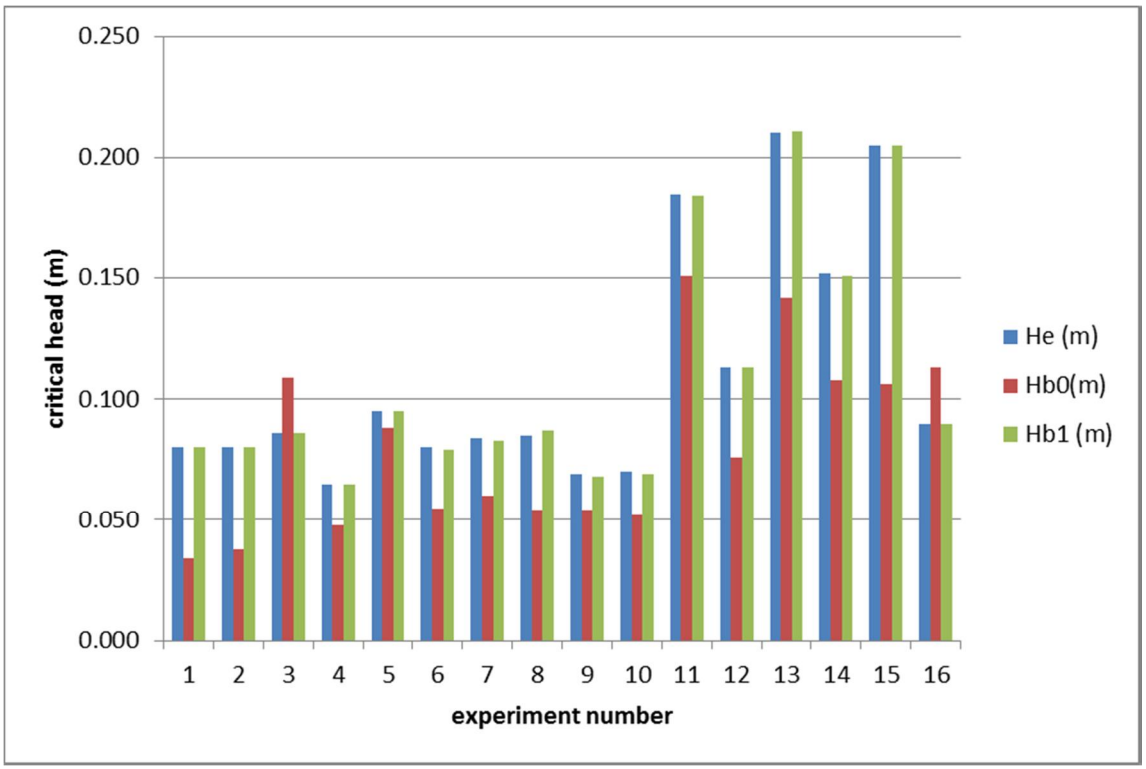

Figure 3.25 Critical head for mean and calibrated pipe width versus measured heads.

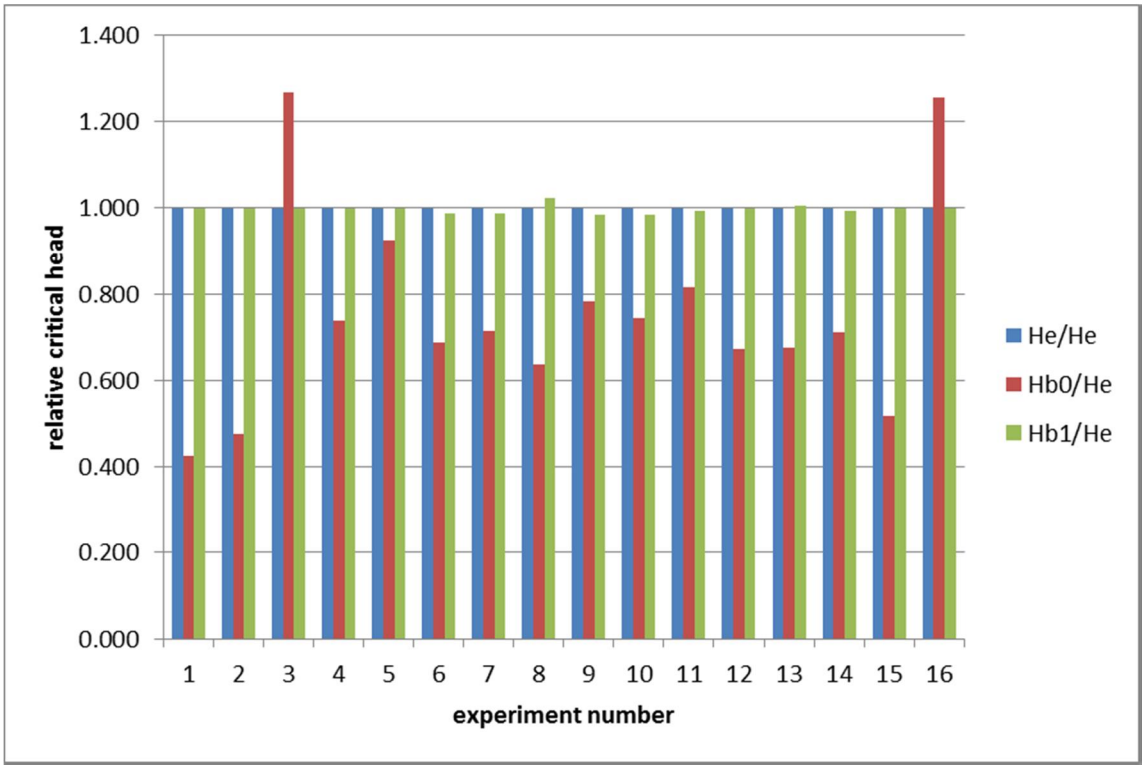

Figure 3.26 Critical head for mean and calibrated pipe width relative to measured heads.

Primary erosion formulation

Table 3.6 presents the critical head that was obtained by 3D DgFlow simulations including primary erosion next to the measured heads. The effect of primary erosion was simulated by putting a criterion on the groundwater head gradient over the not yet activated element next to the tip element. Computations were carried out on the fine element mesh and the bedding angle was set to 37 degrees. In general the medium mesh produced different results than the fine mesh so convergence of the solution could not yet be satisfied. A local refinement procedure has to be added to the code in order to make more accurate computations feasible. Only if this gradient exceeds a certain value (1.50, 1.00, 0.75 or 0.50) then this element becomes active and secondary erosion takes place: the primary erosion criterion thereby increases the critical head over the structure. The table gives a prediction of the critical head gradient criterion in the most right column that was obtained by extrapolation. The results indicate that for most of the experiments a critical head gradient over 2.0 was needed to fit the experimental results on the numerical predictions.

Sand box experiment			**Numerical simulations head gradient criterion**				
nr	Code	H_c(m)	$H_{1.50}$(m)	$H_{1.00}$(m)	$H_{0.75}$(m)	$H_{0.50}$(m)	Dh/dx
1	B115	0.080	0.067	0.050	0.041	0.030	1.88
2	B118	0.080	0.064	0.050	0.043	0.038	2.07
3	W131	0.086	0.157	0.122	0.109	0.109	<0.50
4	B133	0.065	0.073	0.059	0.051	0.048	1.21
5	O140	0.095	0.098	0.090	0.088	0.088	1.31
6	B142	0.080	0.072	0.060	0.055	0.056	1.83
7	B143	0.084	0.084	0.068	0.060	0.060	1.50
8	B144	0.085	0.074	0.060	0.054	0.054	1.89
9	B145	0.069	0.075	0.062	0.055	0.054	1.27
10	B146	0.070	0.075	0.061	0.054	0.052	1.32
11	0163	0.185	0.153	0.153	0.151	0.151	>1.50
12	I164	0.113	0.087	0.078	0.076	0.076	>1.50
13	I166	0.210	0.137	0.137	0.142	0.142	>1.50
14	I167	0.152	0.125	0.109	0.108	0.108	>1.50
15	I168	0.205	0.142	0.107	0.106	0.106	>1.50
16	E169	0.090	0.116	0.115	0.113	0.113	<0.50

Table 3.6 Critical head 3D DgFlow simulations including primary erosion and measured heads (1).

Table 3.7 presents the results of critical head predictions that account for primary erosion in an alternative way. Here the height of the tip element has to overome a critical value ($2.0 \cdot d_{70}$, $3.0 \cdot d_{70}$, $3.5 \cdot d_{70}$, $4.0 \cdot d_{70}$) in order to be activated. The rightmost column of the table presents the critical pipe height criterion based on interpolation. Most of the computations indicate that this critical value should be less than twice the characteristic grain size diameter, Table 3.7 gives an indication of the d_{70} factor if interpolation or extrapolation based on the computational results is possible. If not then < 2.0 is written.

Sand box experiment			**Numerical simulations pipe height criterion**				
nr	Code	H_c(m)	$H_{2.0}$(m)	$H_{3.0}$(m)	$H_{3.5}$(m)	$H_{4.0}$(m)	d_{70} factor
1	B115	0.080	0.042	0.067	0.077	0.104	3.56
2	B118	0.080	0.050	0.085	0.101	0.140	2.43
3	W131	0.086	>0.25	>0.25	>0.25	>0.25	<2.0
4	B133	0.065	0.076	0.140	0.168	0.235	1.91
5	O140	0.095	>0.25	>0.25	>0.25	>0.25	<2.0
6	B142	0.080	0.119	0.238	>0.25	>0.25	1.84
7	B143	0.084	0.103	0.195	0.236	>0.25	1.90
8	B144	0.085	0.132	>0.25	>0.25	>0.25	<2.0
9	B145	0.069	0.091	0.179	0.213	>0.25	1.88
10	B146	0.070	0.079	0.147	0.176	0.246	1.24
11	0163	0.185	>0.25	>0.25	>0.25	>0.25	<2.0
12	I164	0.113	>0.25	>0.25	>0.25	>0.25	<2.0
13	I166	0.210	>0.25	>0.25	>0.25	>0.25	<2.0
14	I167	0.152	>0.25	>0.25	>0.25	>0.25	<2.0
15	I168	0.205	>0.25	>0.25	>0.25	>0.25	<2.0
16	E169	0.090	>0.25	>0.25	>0.26	>0.25	<2.0

Table 3.7 Critical head 3D DgFlow simulations including primary erosion and measured heads (2).

4 Conclusions

Verification tests show the resemblance of numerical computations and the outcome of Sellmeijer's rule for a two dimensional flow problem that was solved in a three-dimensional flow domain. Validation tests compare the outcome of the 2D Sellmeijer's rule and DgFlow results with laboratory observations. Here Sellmeijer's rule computes a critical head difference that is approximately twice as large as the critical value observed in the laboratory experiments. The DgFlow computations provide a critical value that is about 1.5 times as small as the observed value. Increasing the grain size by a factor 1.5, or increasing the pipe width by a factor 3.4 or decreasing the permeability of the medium by a factor 3.4 increases the computed critical head by a factor 1.5 and provide critical heads that compare better with experimental results. However, the observed parameters are not within this range of this variation. Because of the linear dependency of the critical head with the tangent of the bedding angle, an increase in bedding angle from 37^o to 48^o also gives an increase in critical head by a factor 1.5. The bedding angle of 37^o, which is the standard parameter value today, followed from calibration studies in the past of a 2D model. Adding primary erosion to the model increases the critical head and could give more consistent model predictions. Two alternative strategies where proposed that add primary erosion to the numerical procedure. The first approach sets a criterion on the pressure gradient over the element at the upstream side of the tip of the channel. Here simulations indicate that this gradient should be larger than 1.5 for most of the experiments for the element size used. The second approach sets a criterion on the height of the tip of the channel. For this approach simulations indicate that for most of the experiments the tip height should be less than twice the characteristic grain diameter.

The computations that were discussed in this report show that the model is very sensitive to the grain size diameter. On the field scale there is a large variation in gain size diameters and the DgFlow 3D research version could support a research project for finding a representative grain diameter for classes of sand deposits as a function of the construction length. Adaptive grid refinement should be added to the code next to a tracking algorithm in order to reduce computation time and resources. The DgFlow 3D version could also support functional analysis of engineered solutions for the piping problem like sandboxes or permeable walls that hamper the development of the piping channel. Engineering practice needs a robust tool, a DgFlow 2D analysis is better suited for this purpose than the 3D extension, as a 3D

analysis requires large computational times. A design rule like Sellmeijer's rule may even be preferred; however this rule does not capture more complex geo-hydrological situations.

5 Samenvatting

Dijken beschermen het land tegen overstromingen bij hoge rivierwaterstanden en stijgende zeespiegels. In Nederland zijn waterkeringen vaak met slecht doorlatende klei geconstrueerd en zijn gefundeerd op een zandige ondergrond. Dit soort ondergrond is gevoelig voor een erosieproces dat piping genoemd wordt. Gedurende het pipingproces worden kleine kanaaltjes gevormd die aan de landzijde van de waterkering ontstaan waar water uit de ondergrond sijpelt. Tijdens het erosieproces ontwikkelen de kanaaltjes zich naar de waterzijde van de constructie en bij doorgaande erosie kan de waterkering bezwijken. Het model van Sellmeijer geeft de meest nauwkeurige beschrijving van het piping mechanisme tot nu toe, maar beschrijft niet alle deelprocessen. Om te komen tot een meer gedetailleerde beschrijving van het piping proces is binnen het WTI onderzoeksprogramma het eindige elementen model DgFlow ontwikkeld waarmee tevens het effect van tijdsafhankelijke belastingen en stroming door heterogene velden kan worden gekwantificeerd.

In dit rapport wordt de verificatie en validatie van het DgFlow model beschreven. De verificatietesten tonen een goede overeenkomst tussen modelvoorspellingen en de uitkomsten van de regel van Sellmeijer. De validatie testen op basis van laboratorium proeven daarentegen onderschatten het kritiek verval gemiddeld met een factor 1.5. Het kritieke verval kan met een factor 1.5 worden verhoogd door de korreldiameter met een factor 1.5 te vergroten, de breedte van de pipe met een factor $(1.5)^3$ te verhogen of de doorlatendheid van het medium met een factor $(1.5)^3$ te verlagen. De geobserveerde korreldiameter, breedte van de pipe en doorlatendheid van het medium rechtvaardigen een dergelijke aanpassing niet en daarom wordt in dit onderzoek naar het effect van primaire erosie aan de tip van het kanaal in rekening gebracht. Dit proces zal het kritiek verval eveneens doen toenemen. In het rapport wordt een methode gepresenteerd waarmee primaire erosie kan worden beschreven. Het model is daarbij tevens uitgebreid met en criterium voor de breedte - hoogte verhouding van het piping kanaal bij secondaire erosie.

Notations

a	Height of the erosion channel (m)
d	Particle diameter (m)
d_{70}	70 -particle diameter field (m)
d_{70m}	70-particle diameter lab (m)
D	Aquifer thickness (m)
F_g	Geometry term (-)
F_r	Resistance term (-)
F_s	Scale term (-)
g	Gravitational acceleration (m/s^2)
H_c	Critical head difference (m)
K	Hydraulic conductivity (m/s)
l	Actual piping length (m)
L	Potential piping length (m)
N_b	Base functions (-)
p	Pore pressure (N/m^2)
q	Specific discharge (m/s)
$\overline{q}$	Sink term (1/s)
Q	Erosion channel discharge (m^2/s)
W_a	Weighting functions ((-)
y	Elevation level (m)
α	Erosion channel slope (m)
α	Compressibility soil skeleton (m^2/N)
β	Compressibility pore water (m^2/N))
γ^p	Submerged unit weight (N/m^3)
γ^w	Unit weight water (N/m^3)
Γ	Flow domain boundary (m)
η	White's constant (-)
ϑ	Bedding angle (deg)
κ_{ij}	Intrinsic permeability (m^2)
λ	Lamè's constant (N/m^2)
μ	Dynamic viscosity water (Ns/m^2)
ν	Lamè's constant (N/m^2)
ρ^w	Density water (kg/m^3)
ϕ	Hydraulic head (m)
Ω	Flow domain (m^2)

Bibliography

Aziz, K. and A. Settari, 2002. Petroleum Reservoir Simulation. Blitzprint Ltd., Calgary, Alberta.

De Wit, J. M., 1984. Onderzoek Zandmeevoerende Wellen - Rapportage Modelproeven, vol. 220887/10. Grondmechanica Delft.

Hanses U (1985) Zur Mechanik der Entwicklung von Erosionskanälen in geschichtetem Untergrund unter Stauanlagen. Dissertation Grundbauinstitut der Technischen Universität Berlin, Germany.

Huyakorn, P. S. and G. F. Pinder, 1983. Computational Methods in Subsurface Flow. Academic Press.

Lane, E. W., 1935. “Security from Under-Seepage-Masonry Dams on Earth Foundations.” Transactions of the American Society of Civil Engineers 100 (1): 1235–1272.

Sellmeijer, J. B., 1988. On the mechanism of piping under impervious structures. Ph.D. thesis, Delft University of Technology, Delft, The Netherlands.

Sellmeijer, J. B., J. Lopez de la Cruz, V. M. Van Beek and J. G. Knoeff, 2011. “Fine-tuning of the piping model through small-scale, medium-scale and IJkdijk experiments.” European Journal of Environmental and Civil Engineering 15 (8): 1139–1154.

Van Beek, V.M., Van Essen, H., Bezuijen, A., 2014a, Developments in modeling of backward erosion piping, to be published

Van Beek, V.M., Vandenboer, K., Bezuijen, A., 2014b, Influence of sand type on pipe development in small- and medium-scale experiments, ICE7.

Van Beek, V.M., Van Essen, H.M., Vandenboer, K., Bezuijen, A., Geotechnique 65 (9): 740-754, 2015.

Van Esch, J. M., J. B. Sellmeijer and D. Stolle, 2013a. “Modeling Transient Groundwater Flow and Piping under Dikes and Dams.” In G. Pande and S. Pietruszczak, eds., Computational Geomechanics (ComGeo III). Taylor & Francis Group.

Van Esch, J. M., J. A. M. Teunissen and D. Stolle, 2013b. “Modeling Transient Groundwater Flow under Dikes and Dams for Stability Assessment.” In G. Pande and S. Pietruszczak, eds., Computational Geomechanics (ComGeo III). Taylor & Francis Group.

Van Esch, J.M., 2014, ‘Flood Defense Assessment Tools for Piping in WTI 2017 -Report 9b. Groundwater Flow Simulator DgFlow 3D Validation piping module’, Deltares report 1209435-006-GEO-0001.

Vogel, T., M. T. Van Genuchten and M. Cislerova, 2001. “Effect of the Shape of the Soil Hydraulic Functions Near Saturation on Variably-Saturated Flow Predictions.” Advances in Water Resources 24: 133–144.

White, C., 1940. “The equilibrium of grains on the bed of a stream.” Proceedings Royal Society (174A): 322–338.

Wolfs, T. F., 2002. Performance of Levee Underseepage Controls: A Critical Review, vol. ERDC/GSLTR-02-19. Michigan State University.

A Sand box data

Nr	Name	Sand type	d70 (mm)	K (m/s)	W_{exp} (mm)
1	B115	Baskarp 1	0.154	$5.43 \cdot 10^{-5}$	1.83*
2	B118	Baskarp 1	0.154	$6.30 \cdot 10^{-5}$	3.06
3	W131	Hoherstall Waalre	0.400	$5.40 \cdot 10^{-4}$	15.30
4	B133	Baskarp 1	0.154	$9.50 \cdot 10^{-5}$	7.67
5	O140	Oostelijke rivierenzand	0.307	$2.00 \cdot 10^{-4}$	11.20
6	B142	Baskarp 1	0.154	$6.20 \cdot 10^{-5}$	9.37
7	B143	Baskarp 1	0.154	$5.50 \cdot 10^{-5}$	6.42
8	B144	Baskarp 1	0.154	$5.30 \cdot 10^{-5}$	9.02
9	B145	Baskarp 1	0.154	$8.00 \cdot 10^{-5}$	8.42
10	B146	Baskarp 1	0.154	$8.00 \cdot 10^{-5}$	6.82
11	O163	Oostelijke rivierenzand	0.307	$1.30 \cdot 10^{-4}$	25.02
12	I164	Itterbeck 125-250	0.278	$1.30 \cdot 10^{-4}$	7.88
13	I166	Itterbeck mixture 1	0.223	$4.60 \cdot 10^{-5}$	22.17
14	I167	Itterbeck mixture 2	0.203	$3.70 \cdot 10^{-5}$	10.16
15	I168	Itterbeck mixture 2	0.203	$2.70 \cdot 10^{-5}$	9.47
16	E169	Enschede sand	0.431	$3.20 \cdot 10^{-4}$	15.55

Table A.1 Width 0.3 m, height 0.1 m, length 0.48 m, hole at 0.344 m.

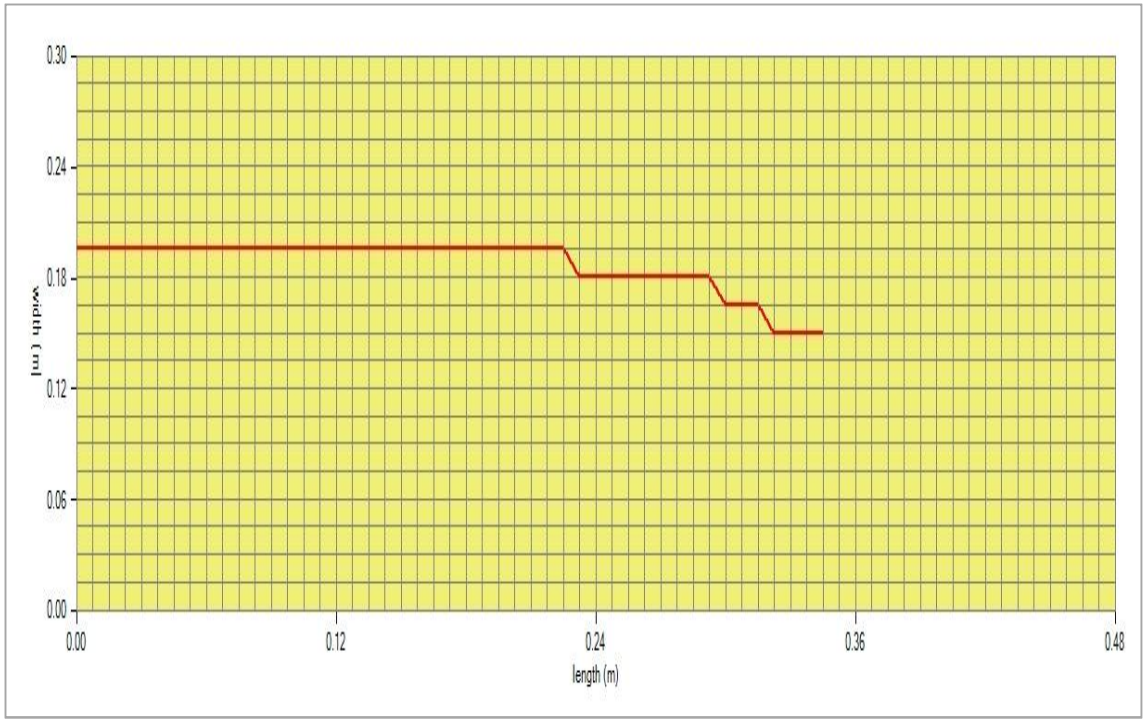

Figure A.1 Experiment B115, pipe track.

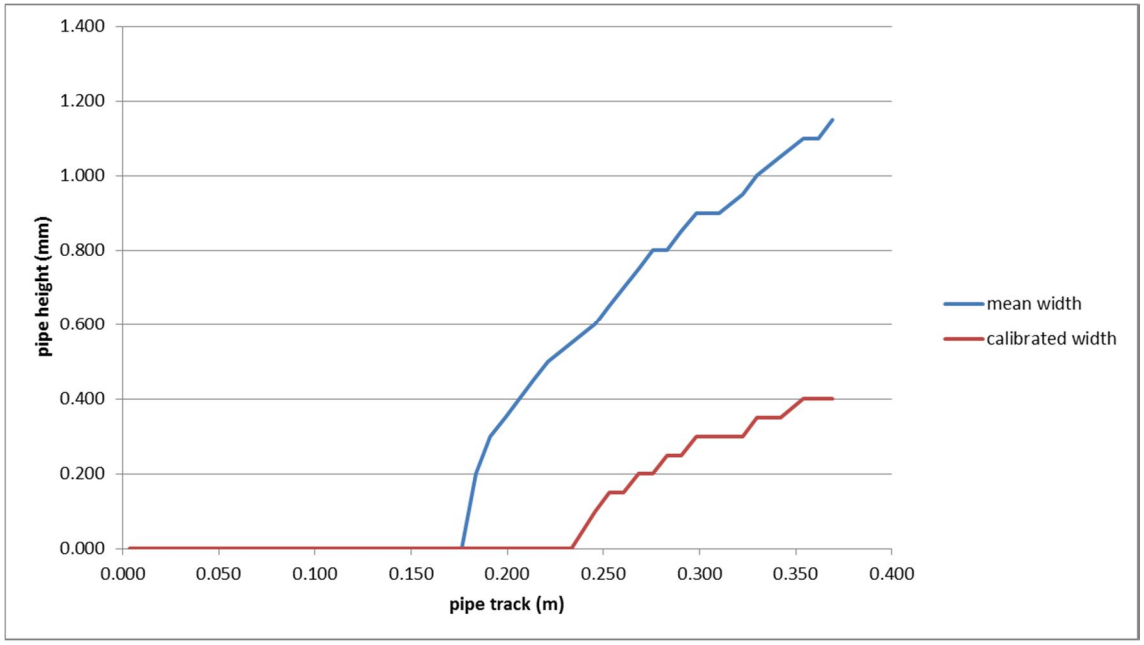

Figure A.2 Experiment B115, critical pipe state.

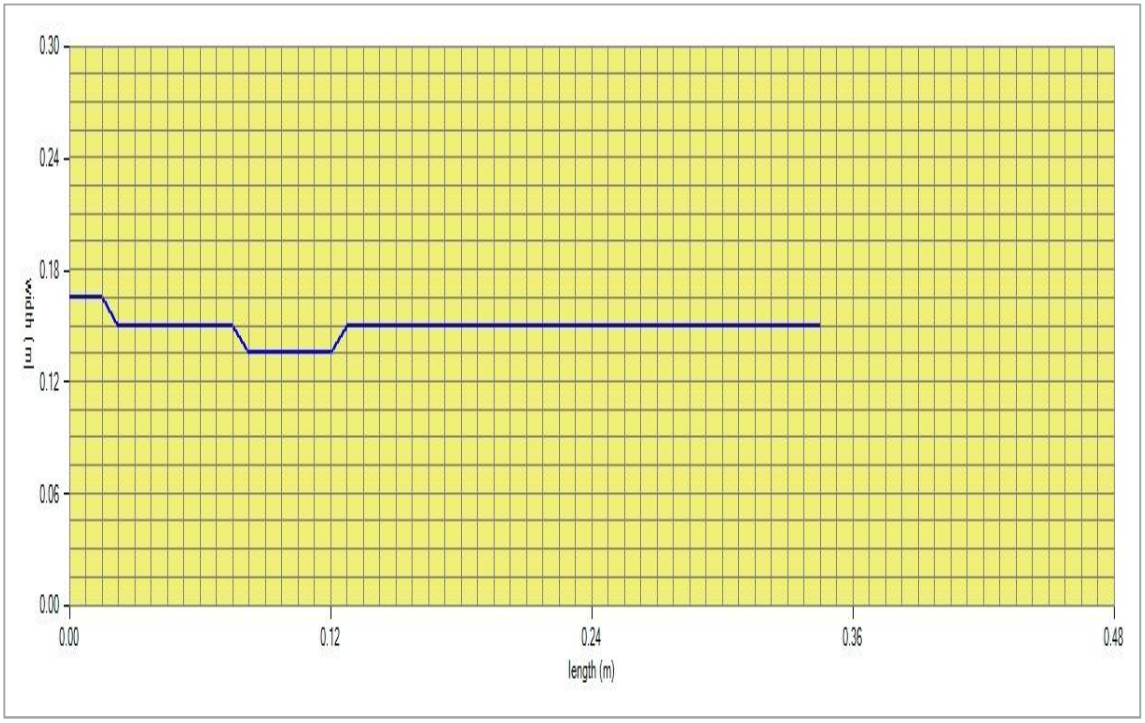

Figure A.3 Experiment B118, pipe track.

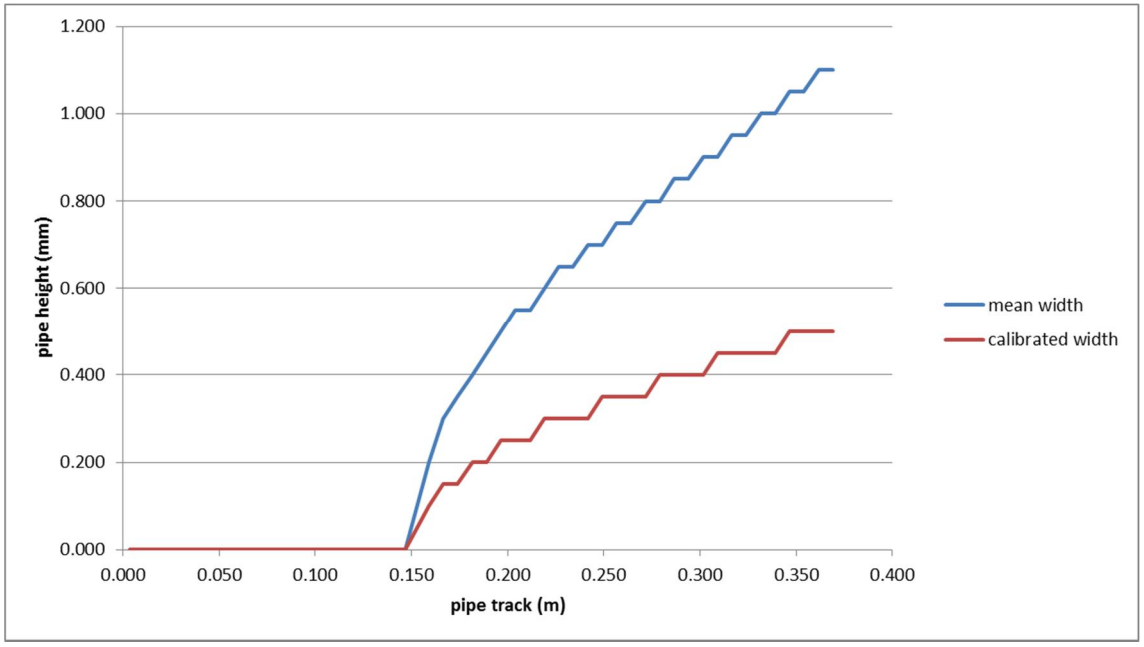

Figure A.4 Experiment B118, critical pipe state.

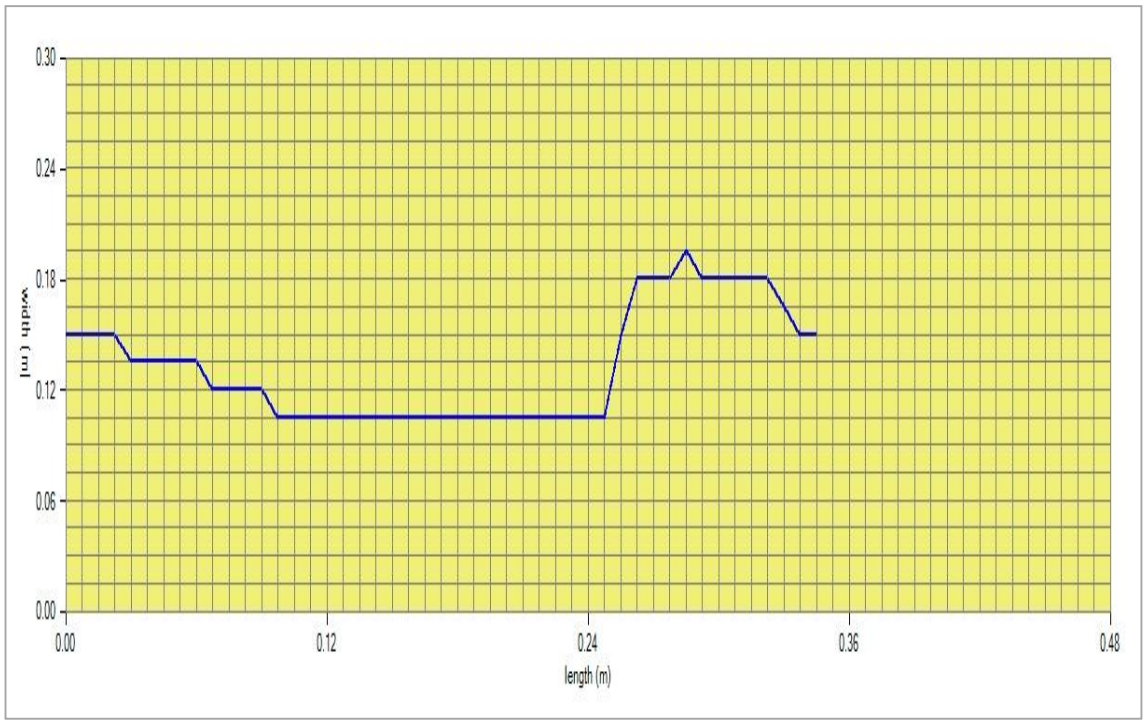

Figure A.5 Experiment W131, pipe track.

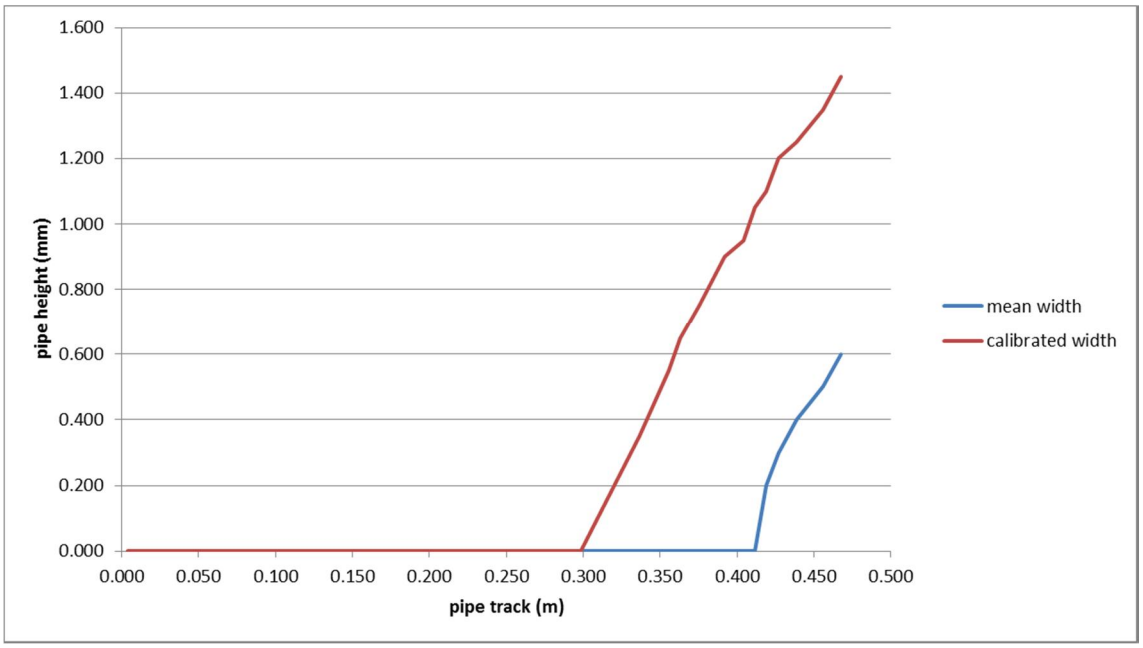

Figure A.6 Experiment W131, critical pipe state.

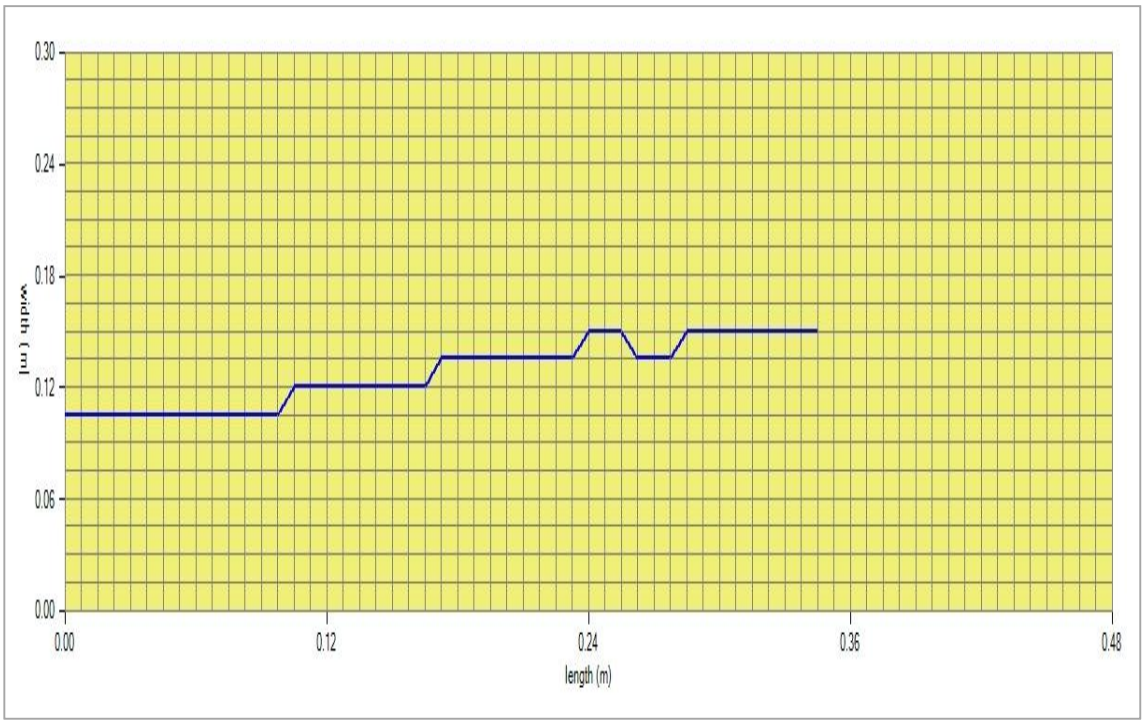

Figure A.7 Experiment B133, pipe track.

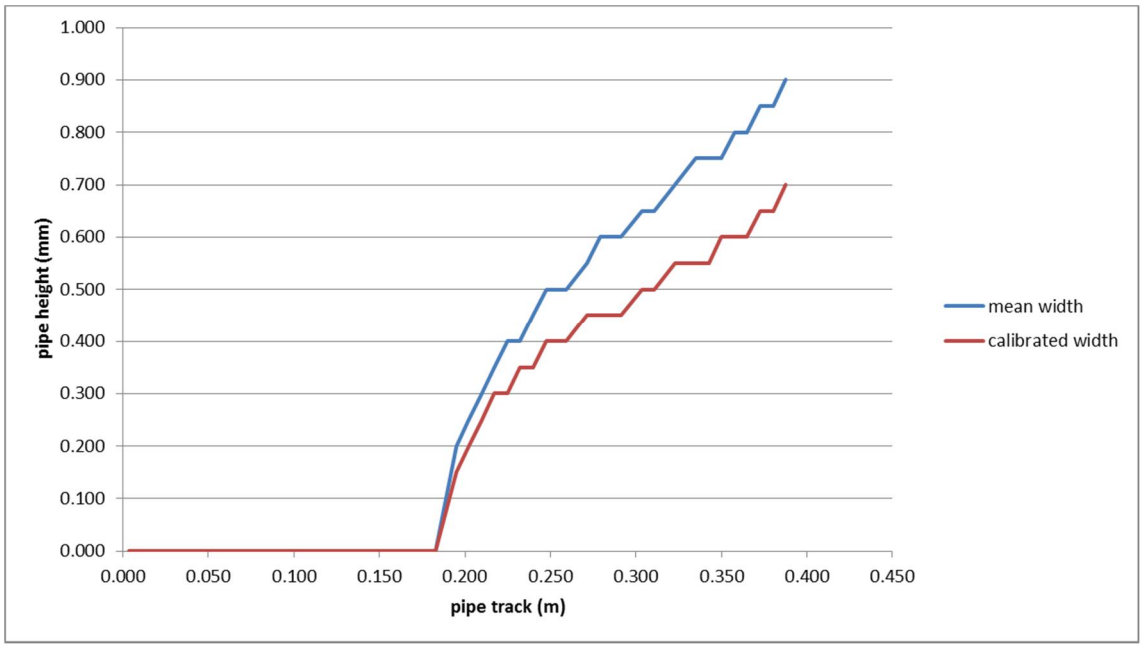

Figure A.8 Experiment B133, critical pipe state.

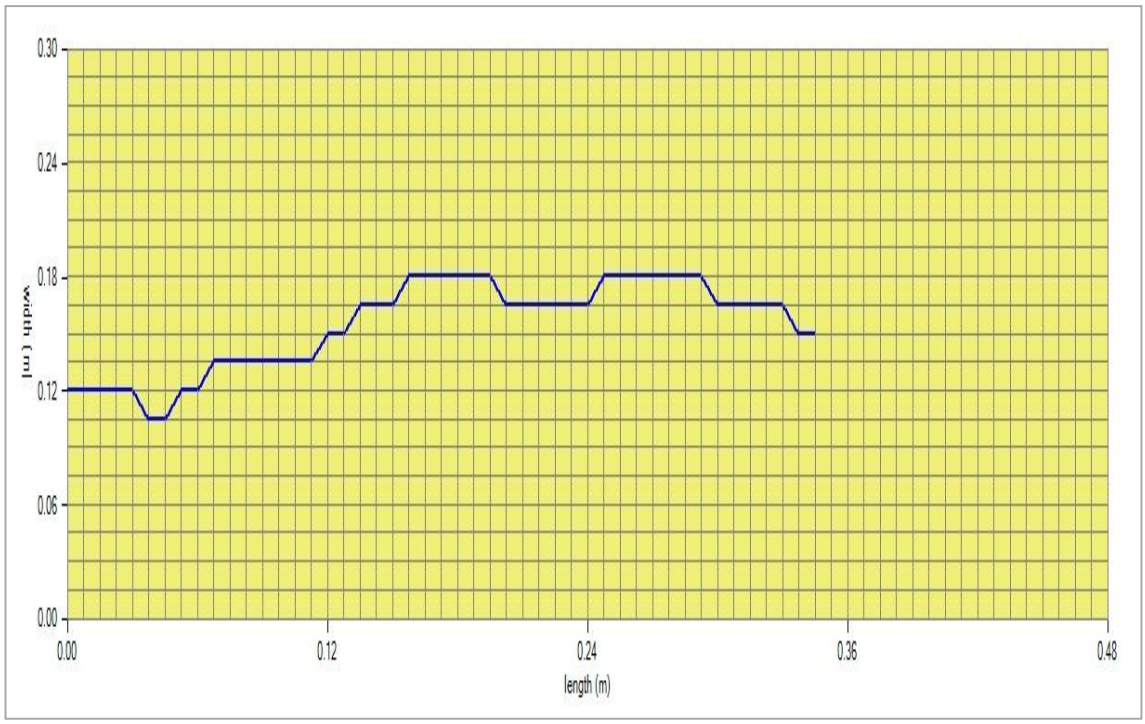

Figure A.9 Experiment O140, pipe track.

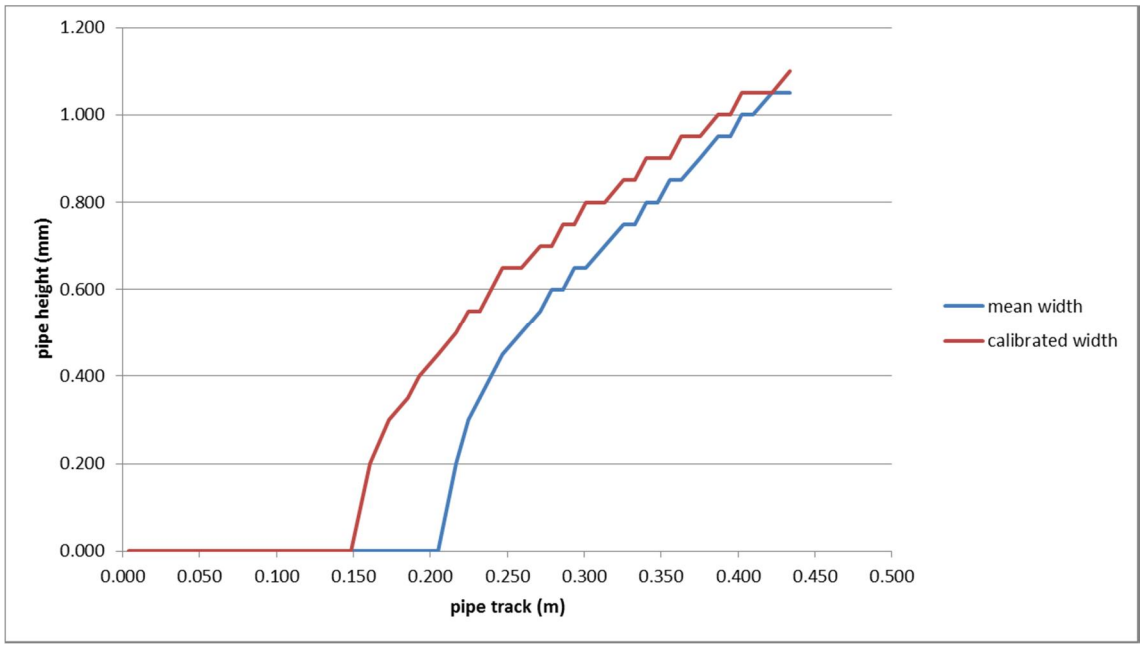

Figure A.10 Experiment O140, critical pipe state.

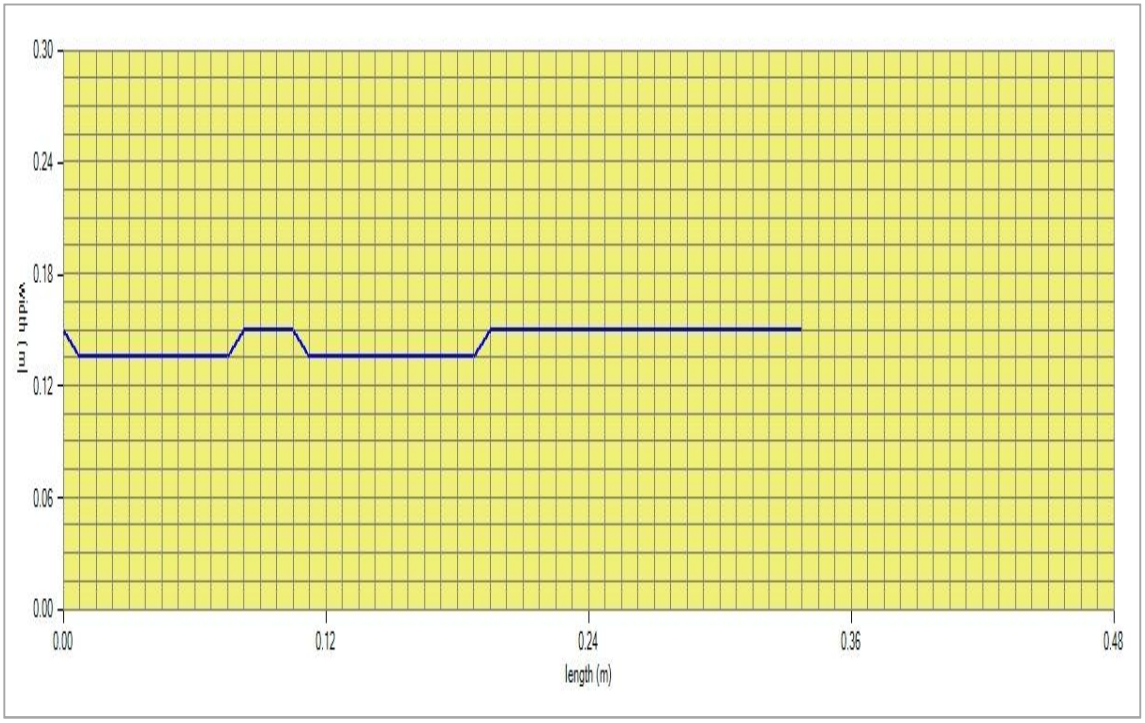

Figure A.11 Experiment B142, pipe track.

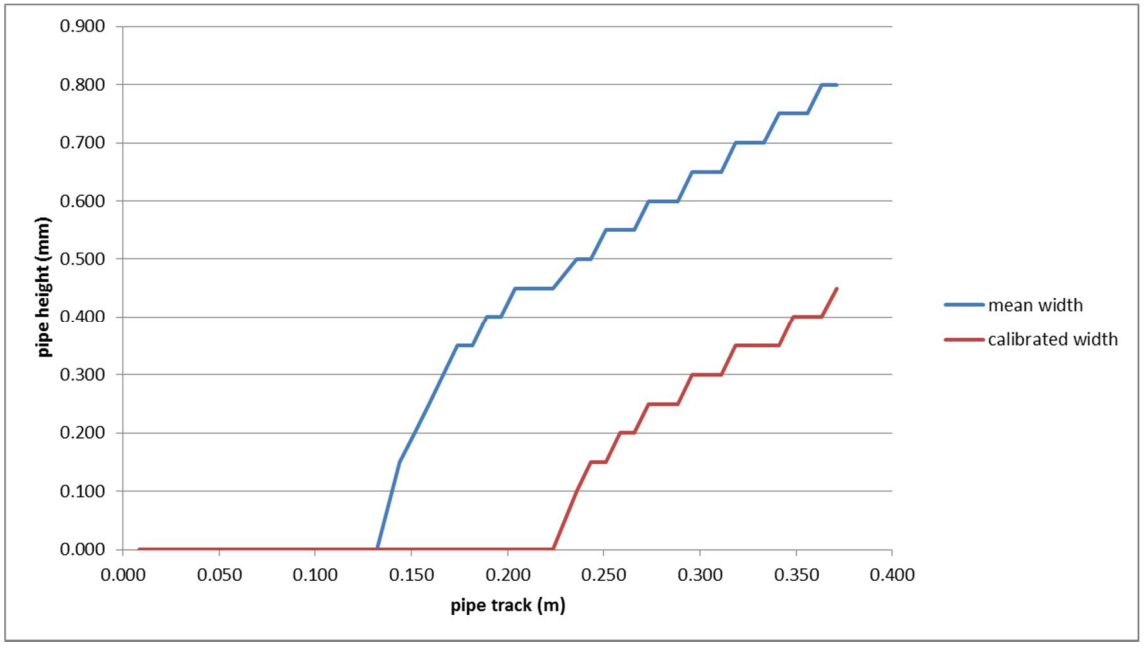

Figure A.12 Experiment B142, critical pipe state.

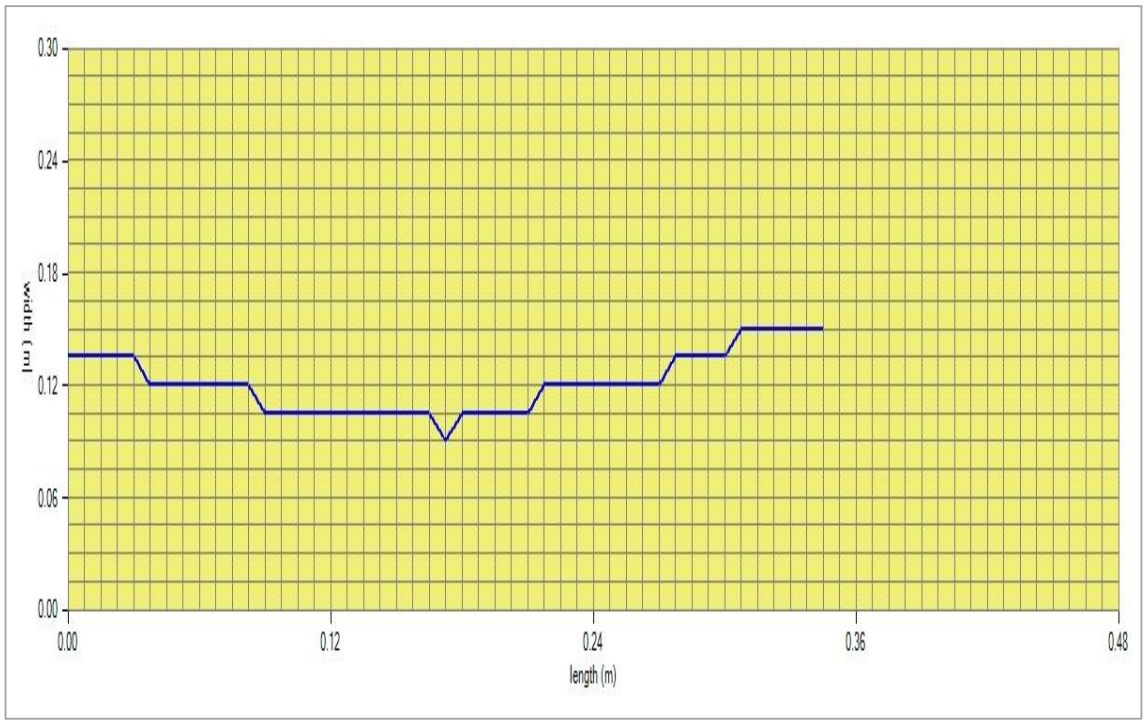

Figure A.13 Experiment B143, pipe track.

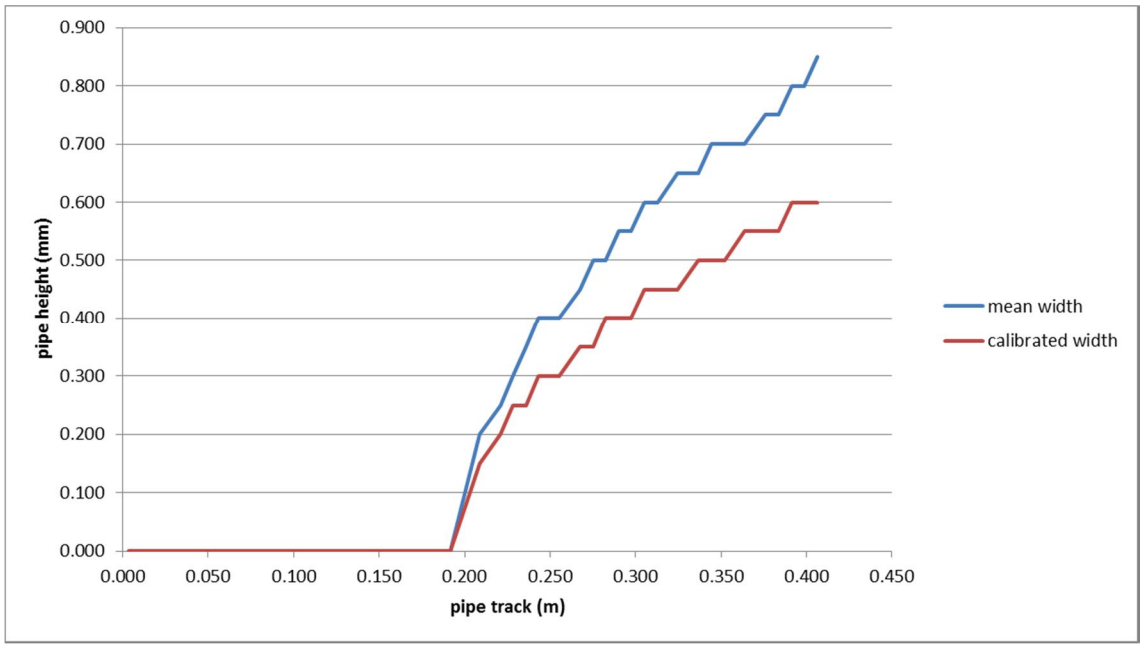

Figure A.14 Experiment B143, critical pipe state.

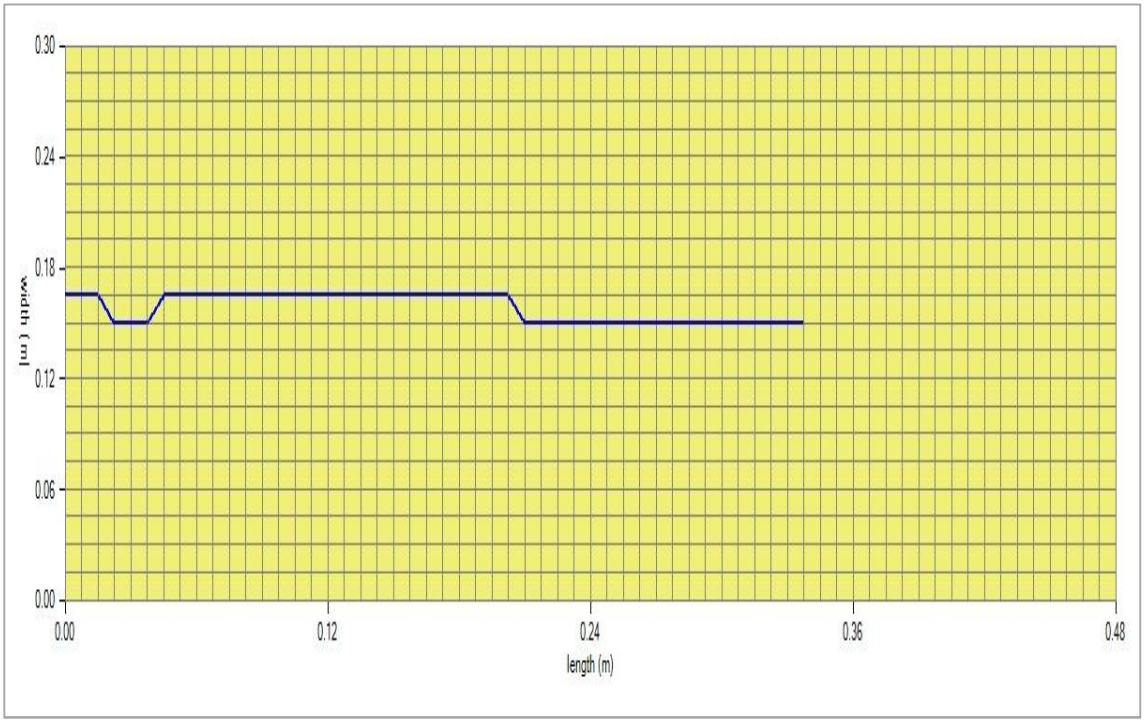

Figure A.15 Experiment B144, pipe track.

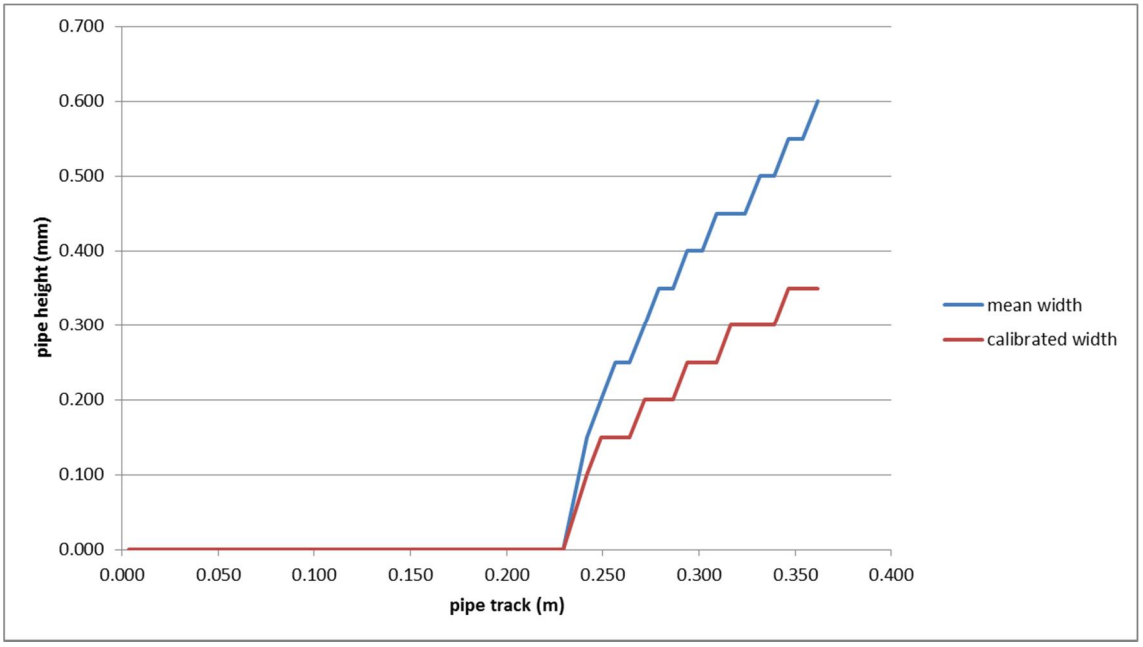

Figure A.16 Experiment B144, critical pipe state.

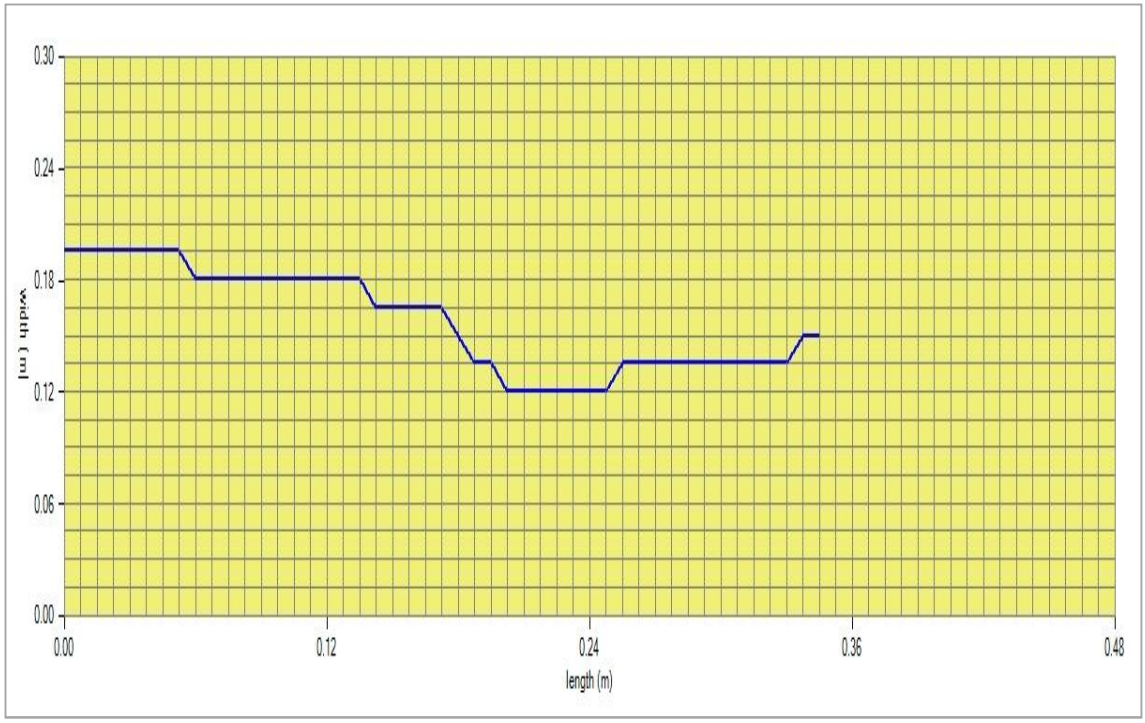

Figure A.17 Experiment B145, pipe track.

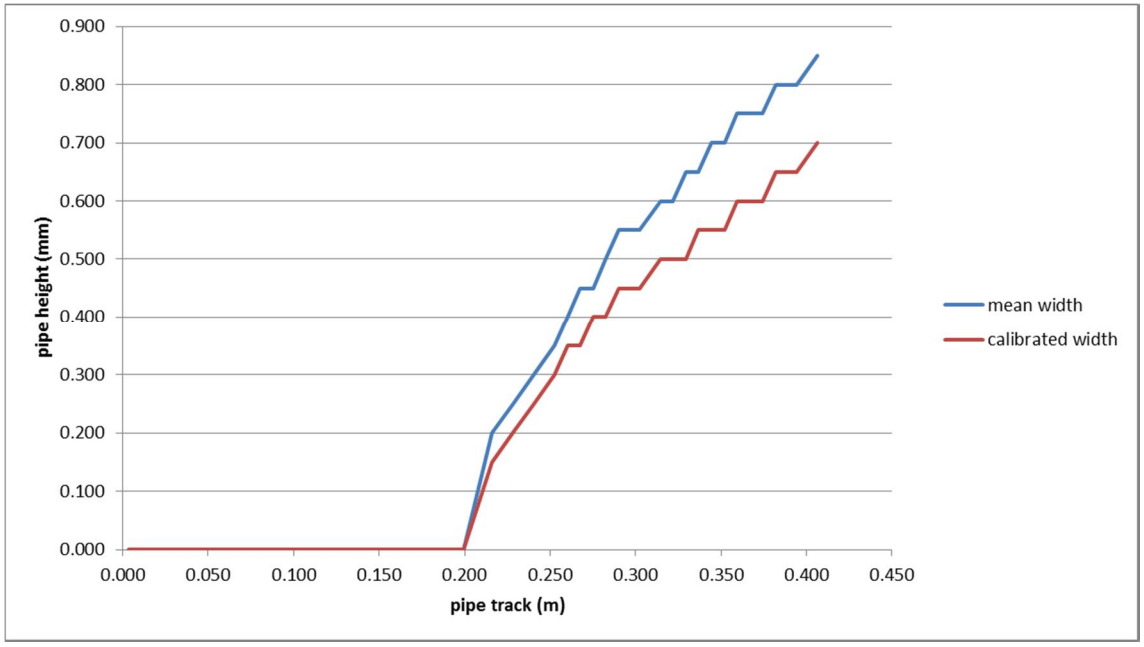

Figure A.18 Experiment B145, critical pipe state.

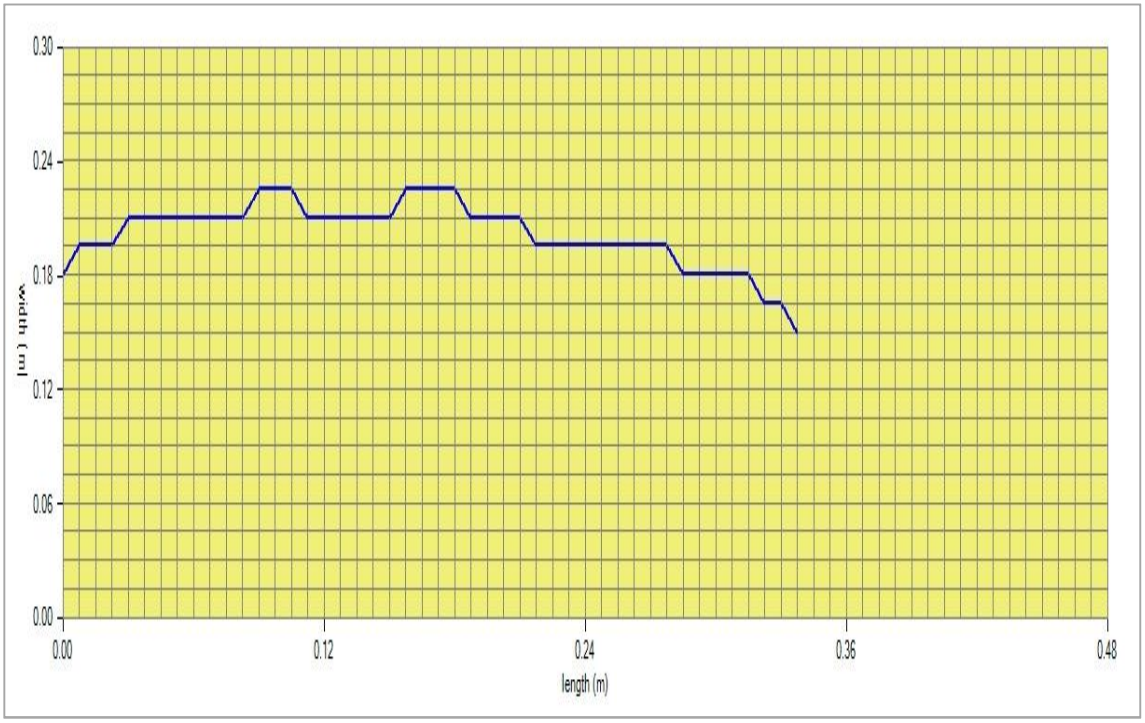

Figure A.19 Experiment B146, pipe track.

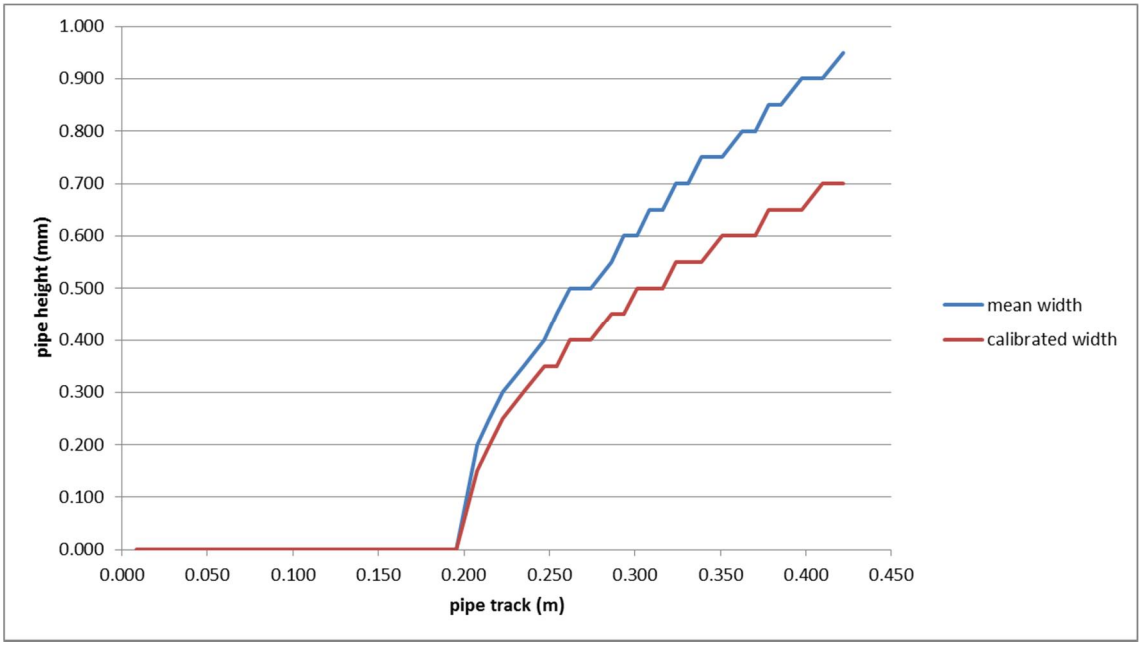

Figure A.20 Experiment B146, critical pipe state.

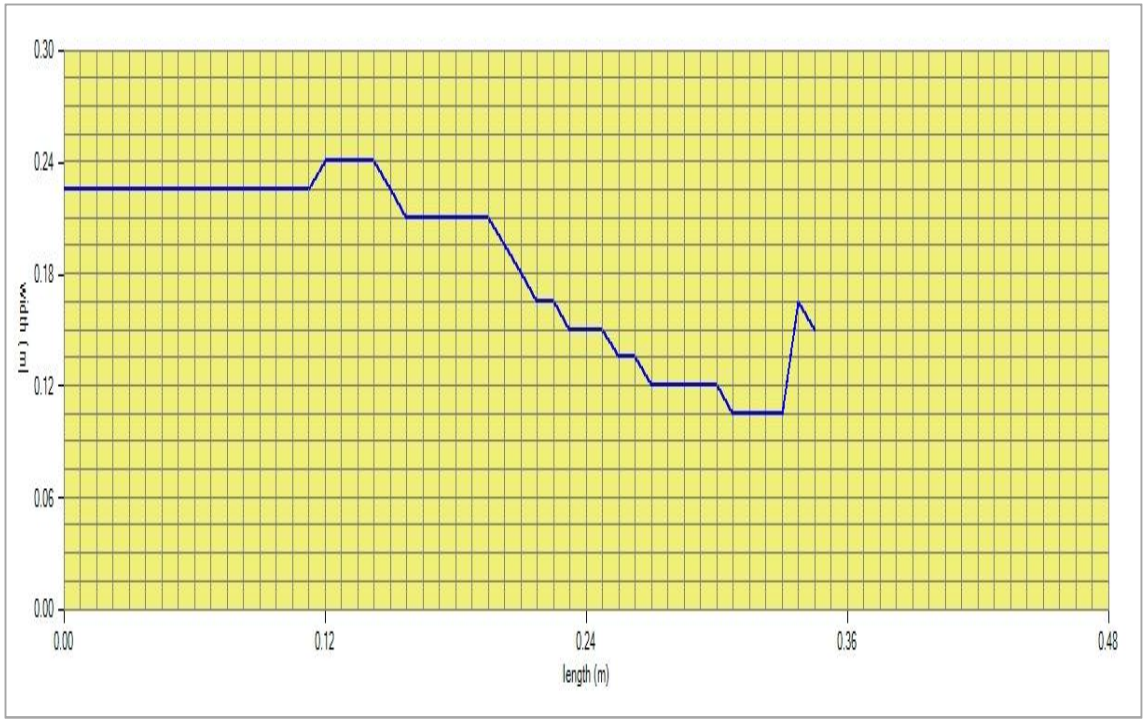

Figure A.21 Experiment O163, pipe track.

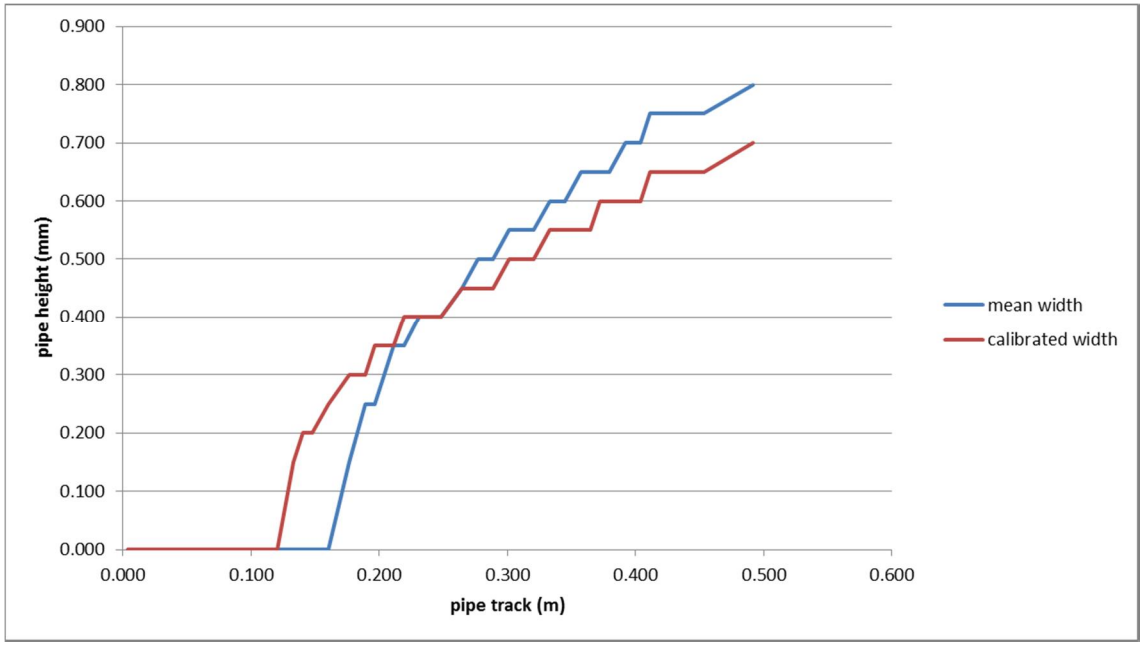

Figure A.22 Experiment O163, critical pipe state.

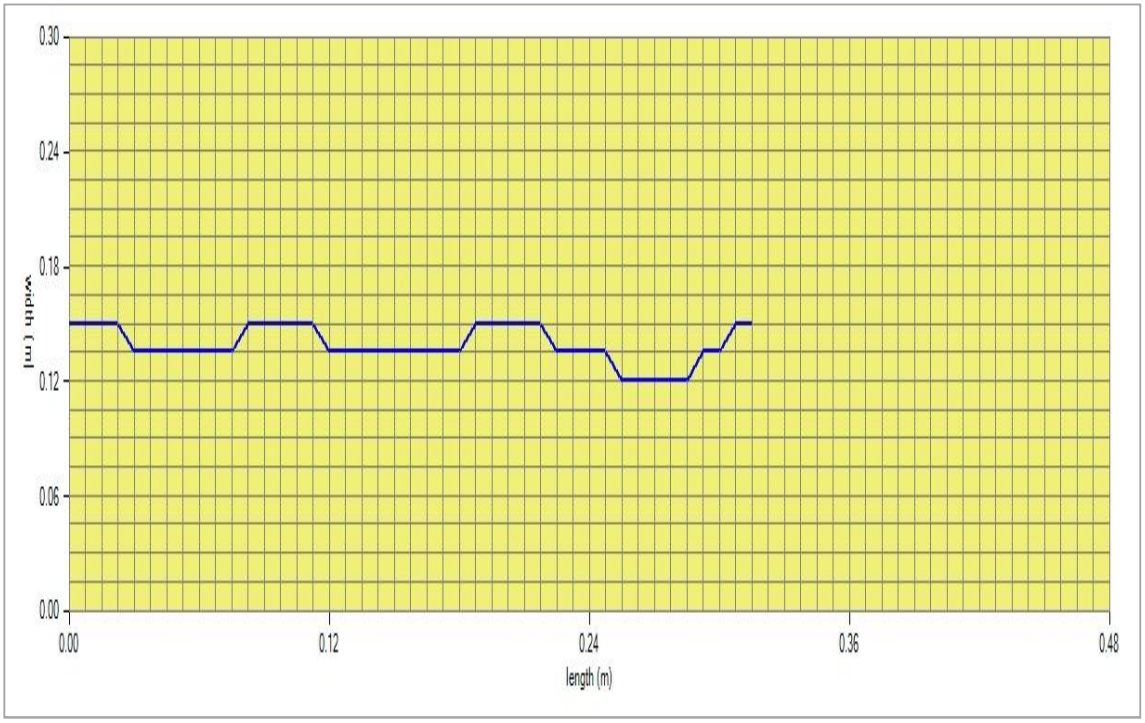

Figure A.23 Experiment I164, pipe track.

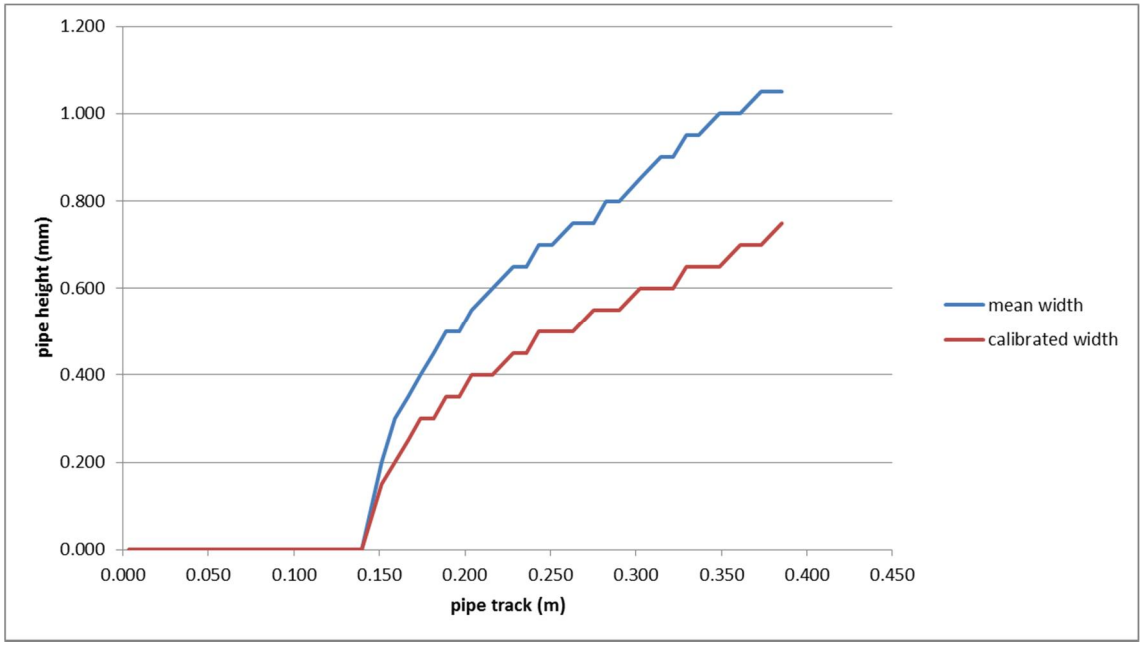

Figure A.24 Experiment I164, critical pipe state.

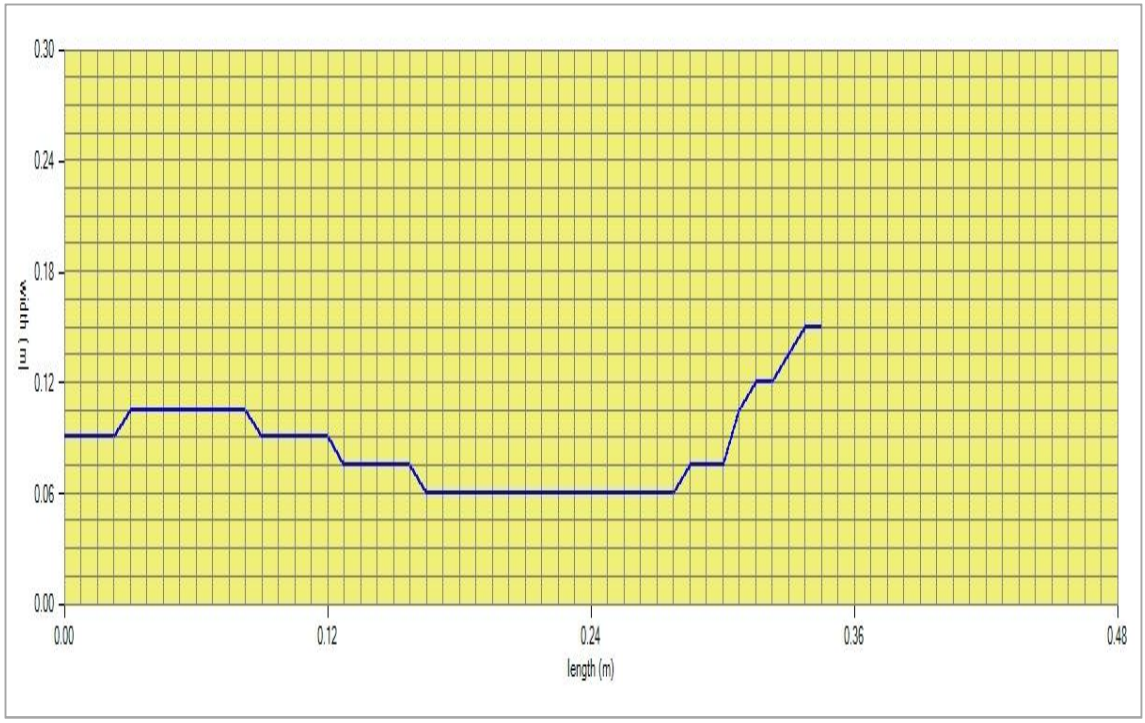

Figure A.25 Experiment I166, pipe track.

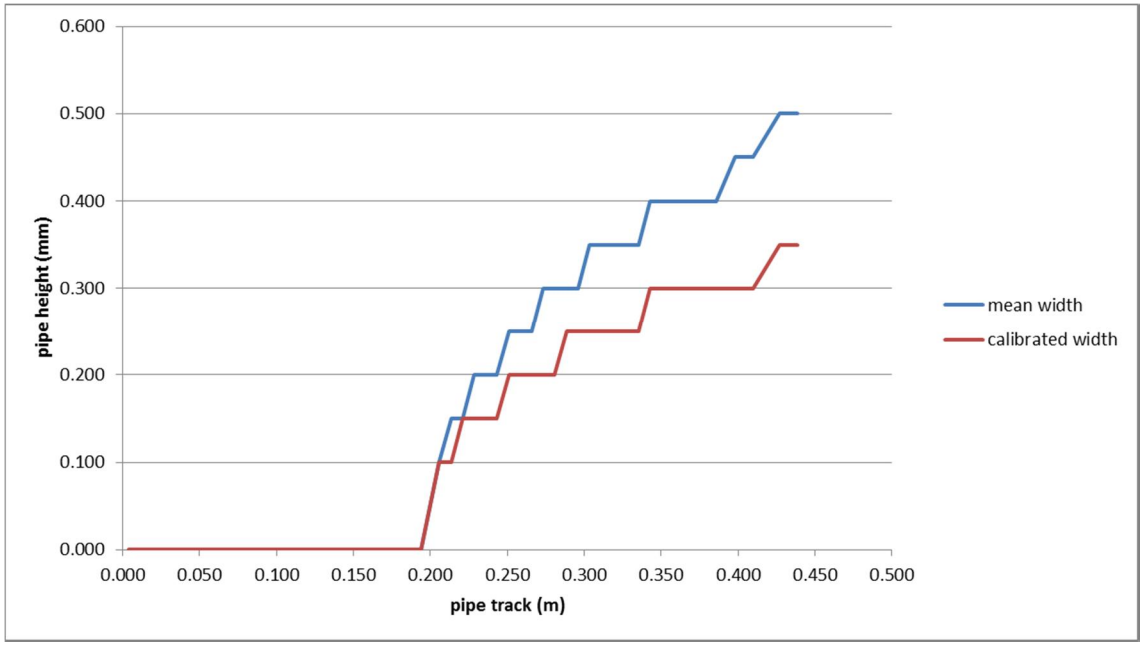

Figure A.26 Experiment I166, critical pipe state.

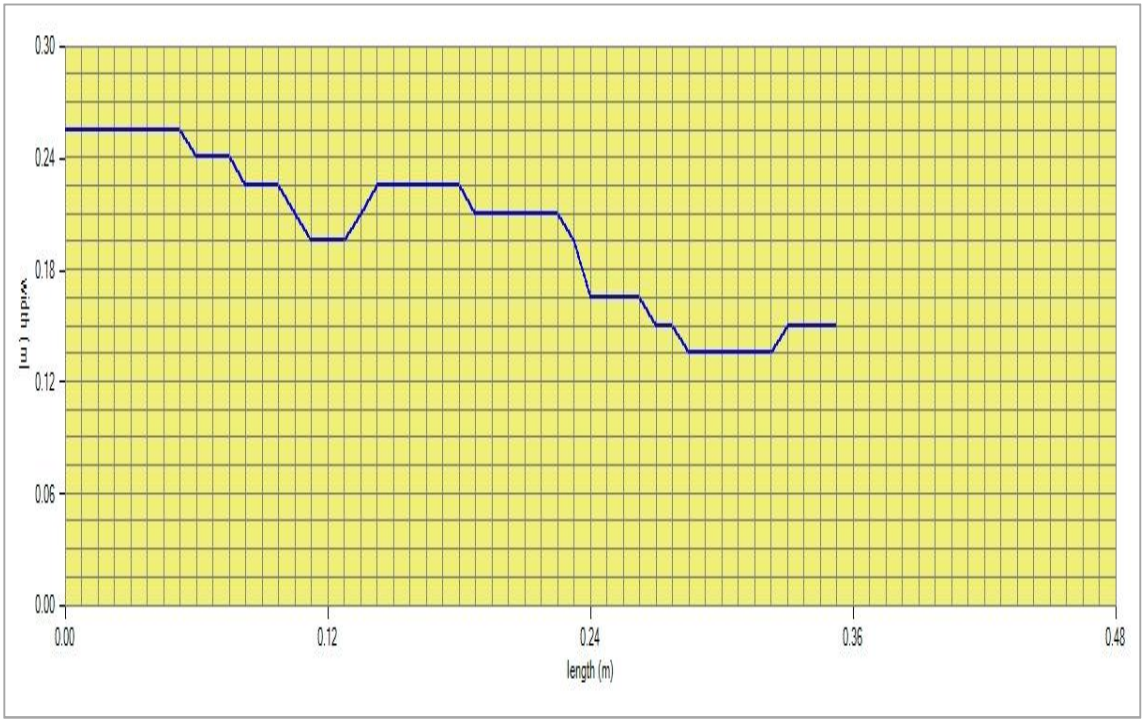

Figure A.27 Experiment I167, pipe track.

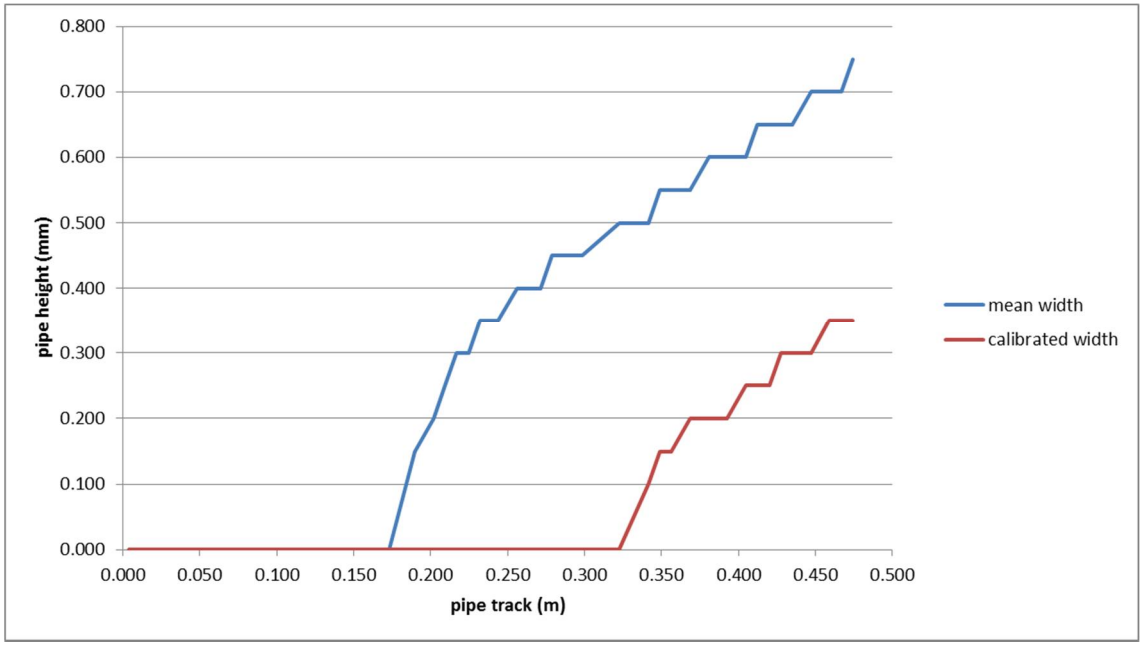

Figure A.28 Experiment I167, critical pipe state.

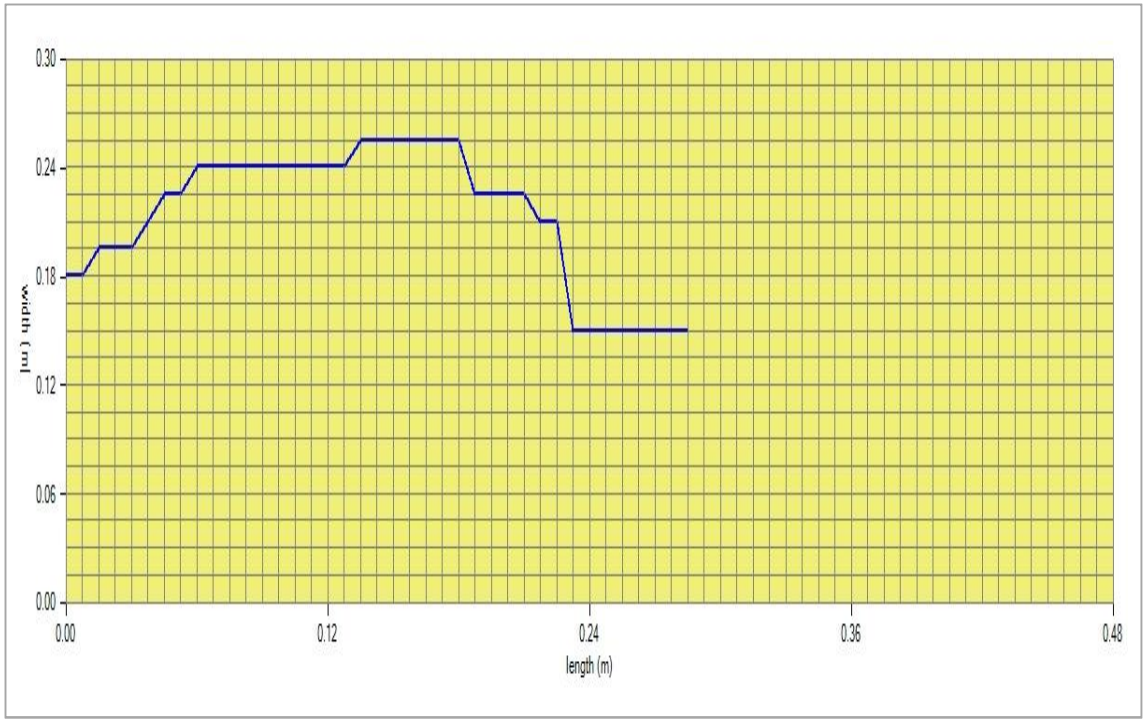

Figure A.29 Experiment I168, pipe track.

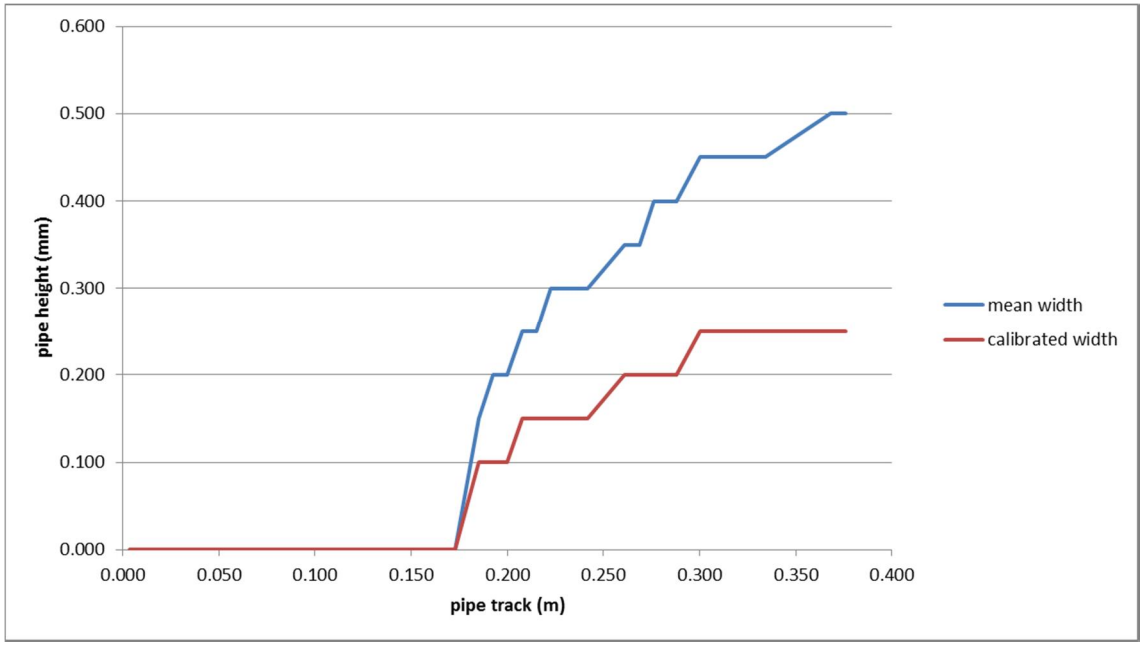

Figure A.30 Experiment I168, critical pipe state.

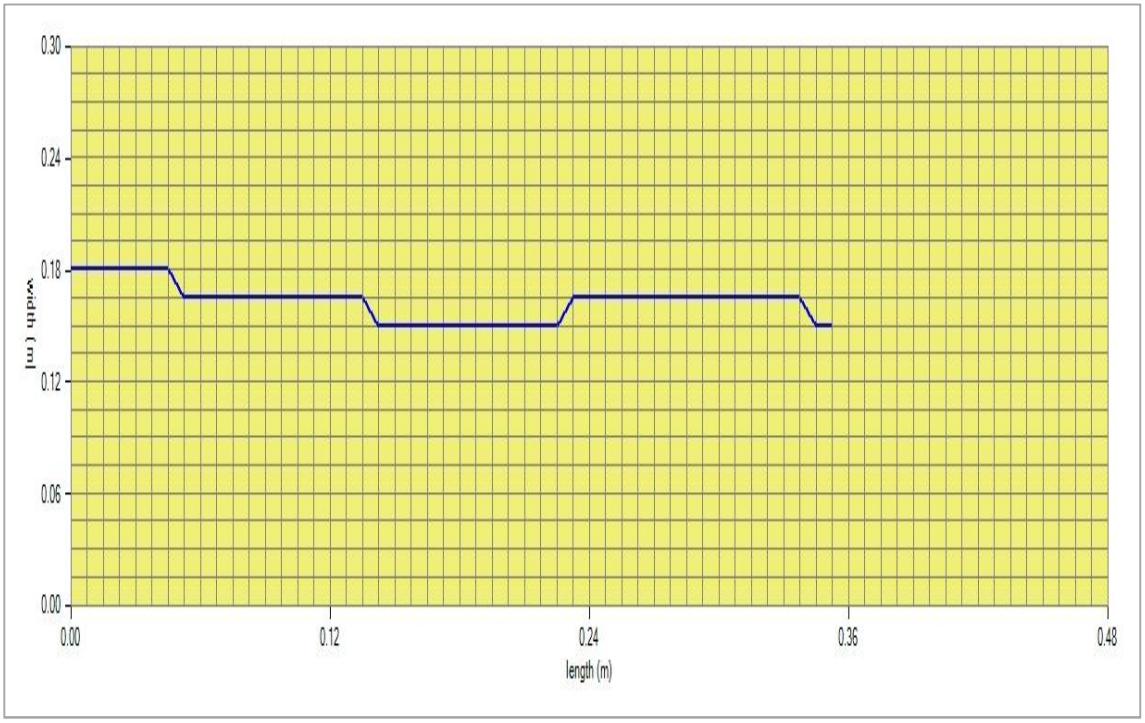

Figure A.31 Experiment E169, pipe track.

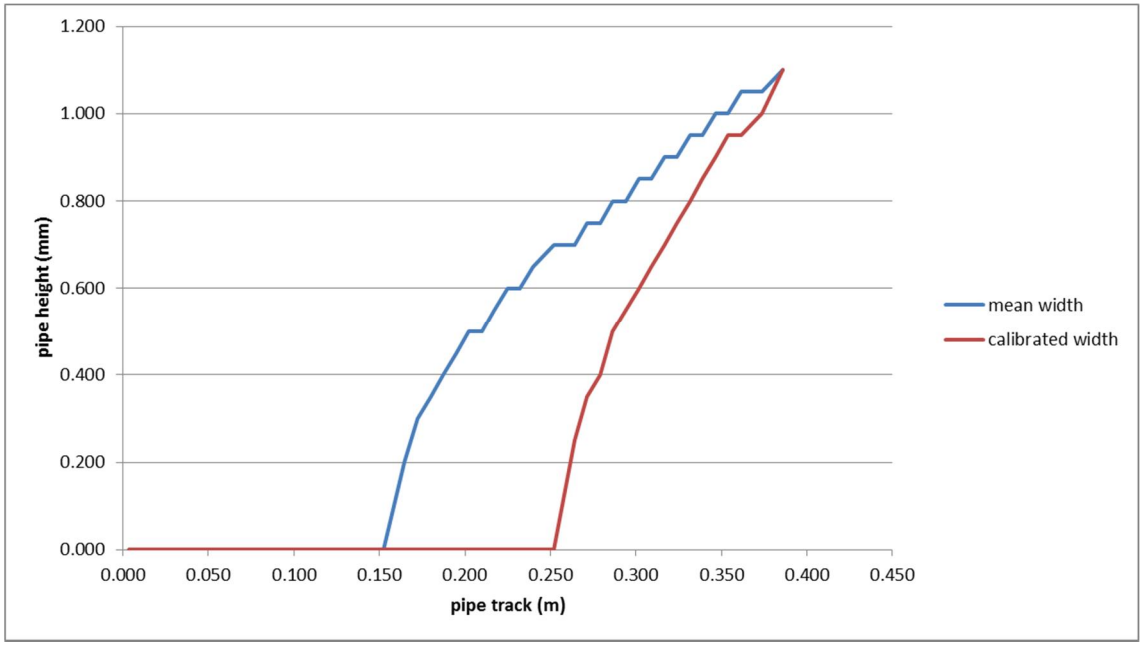

Figure A.32 Experiment E169, critical pipe state.